Austenite stabilization at room temperature in medium Mn DP steels through CPPT

by

Alice Dautezac

Supervisors: Prof. Dr. M.J. Santofimia Navarro & Dr. H. Farahani
Date: September 2023
Faculty: Materials Science & Engineering, Delft

Style: TU Delft Report Style, with modifications by Daan Zwaneveld

TU Delft TATA STEEL

Acknowledgements

I would like to express my deepest gratitude to my supervisors, Prof. Dr. Maria Santofimia Navarro (TU Delft) and Dr. Hussein Farahani (TATA Steel), for their constant support and patience as well as for being a never-ending source of knowledge and expertise. I am also extremely grateful to Prof. Dr. Yaiza Gonzalez Garcia for agreeing to join the defense committee.

Many thanks to all the technicians in the laboratory who helped me during my experiments. In particular, I acknowledge Richard Huizenga for the XRD analysis, Kees Kwakernaak for the EBSD measurements, and Nico Geerlofs for his help with dilatometry experiments. I am also very grateful to Saskia van der Meer for her continuous help with the administrative parts of the thesis process.

I could not have undertaken this journey without the support of my family. They always know how to make me smile, especially in the difficult moments. Lastly, I would like to thank all the friends I met during this master, who made my life brighter and more interesting.

Abstract

The presence of retained austenite (RA) has been proven beneficial for the formability of Advanced High Strength Steels. Therefore, multiple thermal austenite stabilization methods have been researched, such as Mn-partitioning during intercritical annealing in medium Mn steels. The Cyclic Partial Phase Transformation (CPPT) approach has been successful in obtaining localized Mn-enrichment at the ferrite/austenite interface through cyclic annealings at intercritical temperatures in a medium Mn steel. In this thesis, the possible application of CPPT heat treatments towards interfacial austenite stabilization at room temperature in medium Mn Dual Phase (DP) steels is studied. ThermoCalc modelling and dilatometry measurements were used to determine the optimal CPPT parameters for fully martensitic Fe-Mn-C-Si samples with varying concentrations of manganese. Scanning Electron Microscopy acquisitions of the resulting microstructure showed a strong influence from the initial microstructure. Samples which went through a full austenitization formed coarse martensitic islands and equiaxed ferrite grains. However, samples which were intercritically annealed from a fully martensitic state resulted in fine and elongated ferrite grains surrounded by martensite. X-Ray Diffraction analysis revealed that CPPT treated samples with 2wt.%Mn and 4wt.%Mn had a maximum RA volume fraction of 1wt.% and 4wt.% respectively. Up to 14wt.% of RA was obtained at room temperature through CPPT heat treatments for samples with 6wt.% Mn. This difference in results has been attributed to the concentration spike of Mn at the ferrite/austenite interface characterizing the NPLE austenite growth, as well as to the widening of the Mn-enriched zone through repeated isothermal intercritical annealing cycles. While a relatively high volume fraction of RA has been successfully obtained at room temperature in 6wt.% Mn DP steels, its interfacial morphology could not be confirmed due to the interference of the fine ferrite/martensite microstructure with the Electron Back-Scattered Diffraction analysis.

Contents

List of Figures

List of Tables

1

Introduction

One of the current challenges in the field of materials science is to reduce the environmental impact of production as well as diminish the global consumption of critical materials. A decrease in the quantity of raw materials needed for a given application can be obtained by optimizing their mechanical properties after processing. In the automotive field, this means optimizing steel alloys to keep a high strength and improve their formability, which is a complex problem due to the trade-off between strength and ductility [1]. Currently, Advanced High Strength Steels (AHSS) are best suited to respond to this problem. In particular, Dual-Phase (DP) steels (first generation of AHSS) are frequently used as they are known for their high strength and adequate ductility due to their martensitic-ferritic microstructure, as well as for their affordability. However, they lack the high formability of more recently developed AHSS such as the TRIP or TWIP steels.[1][2]

To increase the ductility and thus the formability of DP steels, an option is to regulate the stabilization of retained austenite (RA) in the microstructure [2]–[4]. RA is characterized by a higher ductility and lower strength than ferrite, but can be subjected to TRansformation Induced Plasticity (TRIP) mechanisms which increase the strength of the steel while keeping a high ductility through a $RA - \alpha'$ transformation. These mechanisms could warrant important progress in microstructure/properties control of DP steels. [2][3][5][6]

The stabilization of austenite at room temperature in steels is generally obtained through heat treatments such as isothermal intercritical annealing for medium Mn steels [7][8], or quenching and partitioning treatments for carbon steels[9][10]. Cyclic Partial Phase Transformation (CPPT) heat treatments have recently been successfully used to control the microstructure of a medium Mn steel, more specifically to suppress bandformation through the enrichment in Mn of the austenite/ferrite interface due to the cyclic intercritical annealing[11]. As the stabilization of austenite at room temperature is enhanced by the presence of high Mn concentrations [3][7], CPPT heat treatments might be effective in controlling the shape and volume fraction of retained austenite present in a medium Mn DP steel at room temperature.

In this thesis, DP steels and the known mechanisms of austenite stabilization are first introduced, followed by an explanation of CPPT heat treatments and their applications. The possibility of using CPPT towards austenite stabilization at room temperature is studied through the design of several CPPT heat treatments based on modelling and experiments. Finally, the results of this study are presented and discussed.

2

State of the art

Dual-Phase (DP) steels are part of the first generation of AHSS and are frequently employed in automotive applications as they are known for their high strength and adequate ductility. Some other characteristic mechanical properties of these alloys are good formability, high strain hardening, high crash resistance, high fracture toughness and excellent weldability [1]. However, they lack the high formability of more recently developed AHSS such as the TRIP or TWIP steels as can be seen in Figure 2.1. The primary reason behind the abundant usage of DP steels in the automotive field despite the existence of more efficient steels is their affordability and their relatively simple processing routes. [1][2]

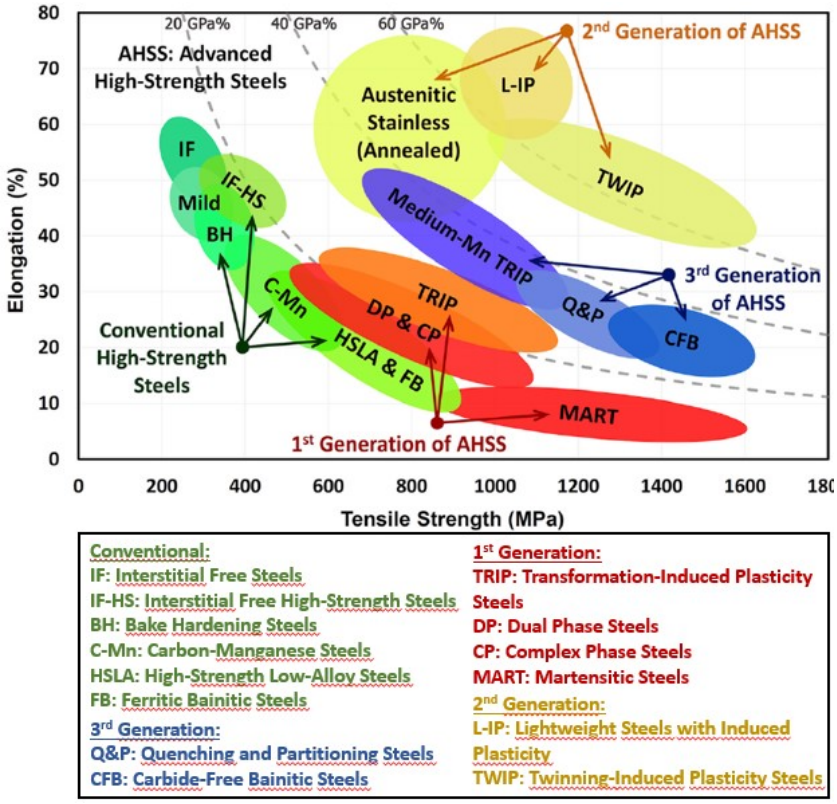

Figure 2.1: Comparison of types of steels based on their elongation and tensile strength.[2]

The dual martensite-ferrite microstructure of DP alloys can be obtained from a low to medium carbon steel through two routes. In route 1 the steel is first isothermally annealed to a temperature T such that $A_1 < T < A_3$, with A_1 and A_3 being respectively the starting and finishing temperatures of the $\alpha \rightarrow \gamma$. This is also called isothermal intercritical annealing and creates an austenite (γ) and ferrite (α)

dual microstructure. Then the steel is quenched, which causes the austenite-martensite transformation $\gamma \rightarrow \alpha'$ and results in the characteristic α-α' microstructure of a DP steel.[1][12]–[14]. Route 2 starts with a full austenitization (γ) of the steel, followed by an intercritical annealing (γ-α) and then quenching to obtain a DP steel microstructure (α-α') [4] [12]–[14]. The mechanical properties of these alloys are dependent on their chemical composition as well as on their microstructure. The volume fractions of α and α', the ferrite grain sizes and the martensite morphologies are the main microstructural parameters affecting the mechanical properties of DP steels.[1][3]

2.1. Retained austenite and TRIP mechanisms

Phases other than α and α' can also be found in small concentrations in DP steels at room temperature. When a steel is heated at temperatures such that $T > A_1$, austenite is formed. When quenched to a temperature inferior to M_s, most of this austenite transforms into ferrite. However, small concentrations of austenite can still be observed at room temperature and this phase is called retained austenite (RA) or austenite stabilized at room temperature [5][15]. The obtained volume fraction of RA at room temperature is dependent on the volume fraction and the chemical composition of the austenite phase during critical annealing. Both these parameters are thermodynamically determined by the intercritical annealing temperature and the initial composition of the alloy [16].

Retained austenite in DP steels can be observed in three different morphologies shown in Figure 2.2: interlath (or capsulated), isolated and blocky [4]–[6][15]. Interlath RA is found inside martensite grains at lath boundaries and in very small quantities, which makes it very difficult to detect [6][15]. It has been found to play an important role in the plastic deformation and ductile fracture of martensitic and multi-phase steels under very low strain rates in uni-axial loading [17]. Isolated RA are RA islands in ferrite grains formed after austenite grains enriched in alloying elements (carbon, manganese) end up trapped by the local growth of ferrite grains [5][15]. The majority of RA grains are blocky and appear at the α/α or α/α' grain boundaries. Their grain size ranges between 1μm and 6 μm [4][18].

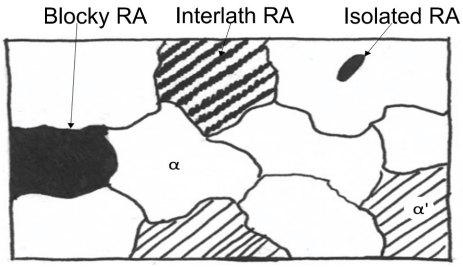

Figure 2.2: Illustration of the different morphologies of RA in DP steels.

The presence of RA will impact the properties of the resulting DP steel as it has a higher ductility and a lower strength than ferrite. TRansformation Induced Plasticity (TRIP) mechanisms also take place in RA, inducing a $RA - \alpha'$ transformation when stress or strain is applied, as illustrated by Figure 2.3. Therefore, the presence of RA in a DP steel gives it a high formability due to its added ductility, and the formation of martensite after deformation increases the strength of the final product [3][5][6]. The TRIP mechanisms can be divided into two categories: Stress-Assisted Martensitic Transformation SAMT and Strain-Induced Martensitic Transformation SIMT.[2]

• **SAMT**: Martensite is usually formed by quenching a partly or fully austenitized steel to a temperature equal or below the martensite start temperature M_s, and is characterized by a critical chemical driving force $\Delta G_{M_s}^{\gamma-\alpha'}$ at M_s. At a higher temperature T_1, the chemical driving force of the $\gamma - \alpha'$ transformation decreases, as illustrated in Figure 2.4a, and becomes insufficient to trigger the phase transformation. By applying stress on the steel, a mechanical driving force U' is generated and added to the chemical driving force $\Delta G_{T_1}^{\gamma-\alpha'}$. The total driving force is now sufficient to trigger the $\gamma - \alpha'$ transformation at a temperature T_1 higher than M_s. Therefore, RA which is stable at T_1 will also transform into martensite under stress at T_1. Figure 2.4b shows that the SAMT mechanism happens for $T \in [M_s, M_s^\sigma]$ and the required stress increases linearly with temperature.[2]

• **SIMT**: For temperatures above $T = M_s^\sigma$, it is more energetically favorable for austenite to plastically

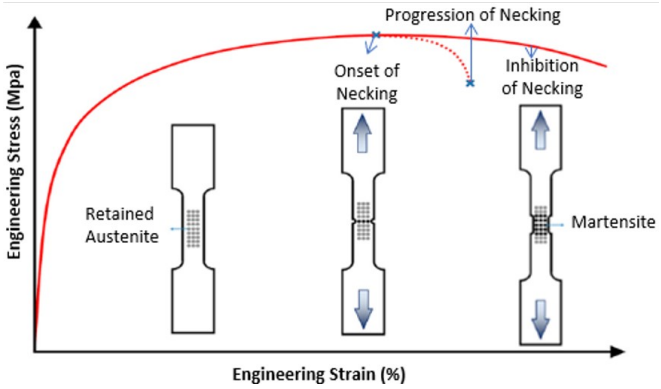

Figure 2.3: Schematic illustration of TRIP effect during tensile deformation.[2]

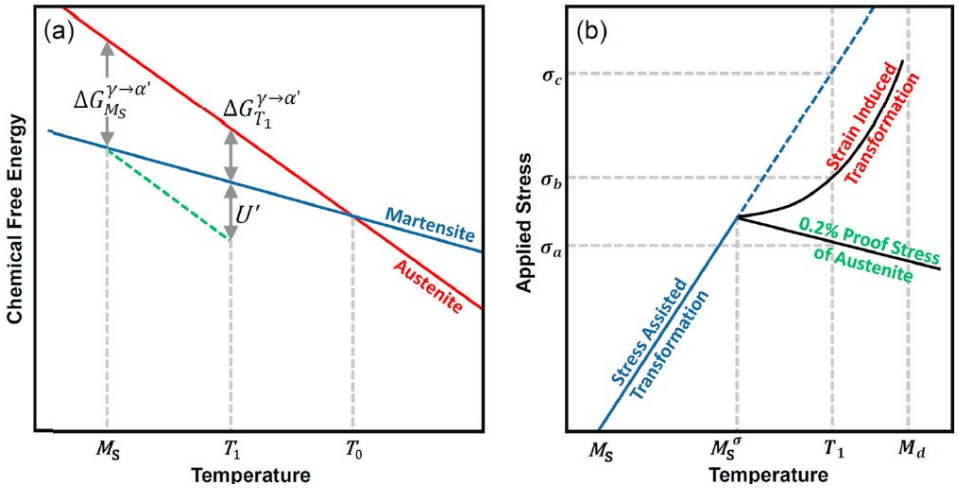

Figure 2.4: (a) Chemical free energies and driving forces of γ and α'. (b) SAMT and SIMT mechanisms depending on temperature.[2]

deform than to transform into martensite when an external stress is applied. The plastic deformation of the austenite grains generates energetically favorable martensite nucleation sites. Therefore, the $\gamma \to \alpha$' transformation is a strain induced transformation, and requires less energy than the SAMT at $T > M_s^\sigma$. This is illustrated in Figure 2.4b, which shows that for $T > M_s^\sigma$ the applied stress necessary to trigger the SAMT mechanism is higher than the stress needed for the SIMT mechanism. The SIMT of austenite to martensite is especially seen in steels with relatively low stacking fault energies due to their chemical composition. [2]

To be able to exploit the benefits of the TRIP mechanisms associated with RA in DP steels, it is necessary to understand the mechanisms leading to RA in steels. In the following, the thermal stabilization of austenite at room temperature through mechanisms such as Mn-partitioning, C-partitioning, and ferrite growth is explained. The expected outcome of CPPT heat treatments as a mean of austenite stabilization at room temperature in DP steels is then developed.

2.2. Austenite stabilization through Mn-partitioning

By heating a medium Mn steel (3-12 Mn wt.%) to an intercritical temperature T ($A_1 < T < A_3$), a dual-phase $\gamma - \alpha$ microstructure is obtained. Since the bulk diffusion kinetics of manganese are higher in austenite than in ferrite, manganese atoms partitions in austenite grains. Therefore, austenite grains have a higher Mn concentration than ferrite grains. Manganese atoms also tend to gather at grain boundaries, as they are the channel of diffusion with the highest kinetics, which results in Mn spikes at $\alpha - \alpha$, $\gamma - \gamma$ and $\alpha - \gamma$ interfaces. As the Mn bulk diffusion at intercritical temperatures remains slow

in austenite, the borders of austenite grains have a higher manganese concentration than their bulk. [7][8][19]

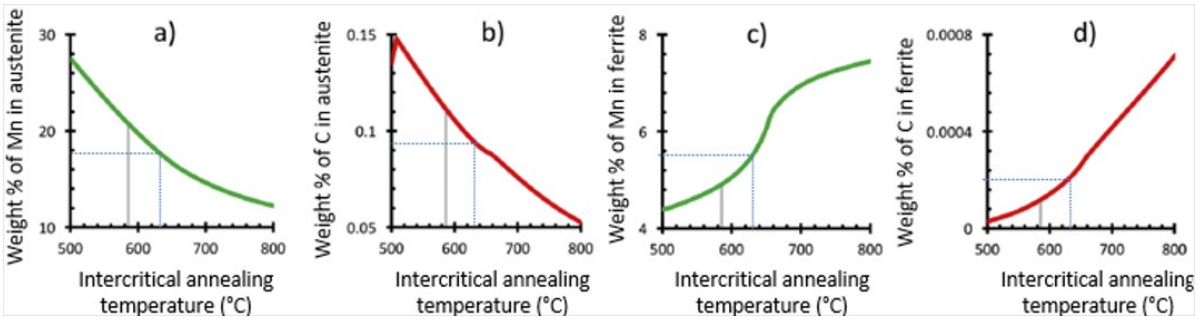

Figure 2.5: Weight percentage of Mn and C in austenite and ferrite at room temperature depending on the annealing temperature.[19]

Annealing allows the alloying elements (Mn, C) to diffuse both through bulk diffusion systems and through grain boundaries and dislocations migration [8]. Figure 2.5 is the result of simulating through ThermoCalc the distribution of carbon and manganese in retained austenite and ferrite grains in a Fe-12Mn-3Al-0.05C (wt.%) alloy at room temperature, depending on intercritical annealing temperatures and for a holding time of 1h. The relation between alloying element content at room temperature and annealing temperature is not linear, as the manganese curves tend to soften after 630°C while the carbon curves seem to harden. Figures 2.5a and 2.5b show that the concentration of C and Mn in retained austenite at room temperature decreases when the intercritical annealing temperature increases. The opposite phenomenon can be seen for ferrite (cf. Figure 2.5c and 2.5d), where the alloying elements concentration keeps on increasing. This is explained by the fact that an increase of the intercritical annealing temperature leads to an increase of the austenite volume fraction and a decrease of the ferrite volume fraction [3][19]. For the system to remain in a thermodynamical equilibrium, the concentrations of C and Mn in austenite decrease [3][16][19]. Mahieu's equation (cf. equation 2.1) relates the martensite start temperature M_s to the alloying elements concentration in wt.% for a Fe-C-Mn-Al-Si alloy [20], and has been successfully used to model the M_s dependency on composition for Fe-Mn-C alloys [7].

$$M_s = 539 - 423C - 30.4Mn - 7.5Si + 30Al \tag{2.1}$$

This equation shows that M_s increases with a decrease of the concentration of Mn and C.[7] Therefore, a sufficiently high intercritical annealing temperature leads to a relatively high M_s, and thus to a higher rate of the $\gamma \rightarrow \alpha$' transformation upon quenching. This explains the decrease in the volume fraction of retained austenite at room temperature shown in Figure 2.6a. Figure 2.6a results from the same simulation as Figure 2.5, and shows the simulated volume fraction of retained austenite at room temperature depending on the annealing temperature. The maximum of the simulated volume fraction of retained austenite for this alloy is 33.5% and is obtained at around 630°C. This corresponds to a retained austenite phase with 18 wt.%Mn and 0.09 wt.%C, as well as a ferrite phase with 5 wt.%Mn and 2.10^{-4} wt.%C as shown in Figure 2.5 [3][19]. These results are a consequence of the higher Mn and C solubility in γ than in α.[19]
Similar results have also been obtained by De Moor et al. in their ThermoCalc simulation of the importance of manganese and carbon partitioning in austenite stabilization depending on intercritical annealing temperature. This time a Fe-5.7Mn-0.11C (wt.%) steel is investigated. Figure 2.6b highlights that Mn-partitioning is the lead mechanism of austenite growth during intercritical annealing in medium Mn DP steels, as the simulated volume fraction of RA at room temperature based on carbon partitioning differs widely from the experimental results. For this alloy, the maximum retained austenite fraction seems to be obtained after annealing for an hour at around 650°C experimentally and at around 600°C in simulation.[21]

Carbon has a higher diffusion rate at the same temperature than manganese. Figure 2.7 shows the consequence of this difference. In this simulation, a Fe-5Mn-0.2C-1.5Al (wt.%) steel is annealed at 680°C for different annealing times. It can be seen that the concentration peak of carbon at the interface

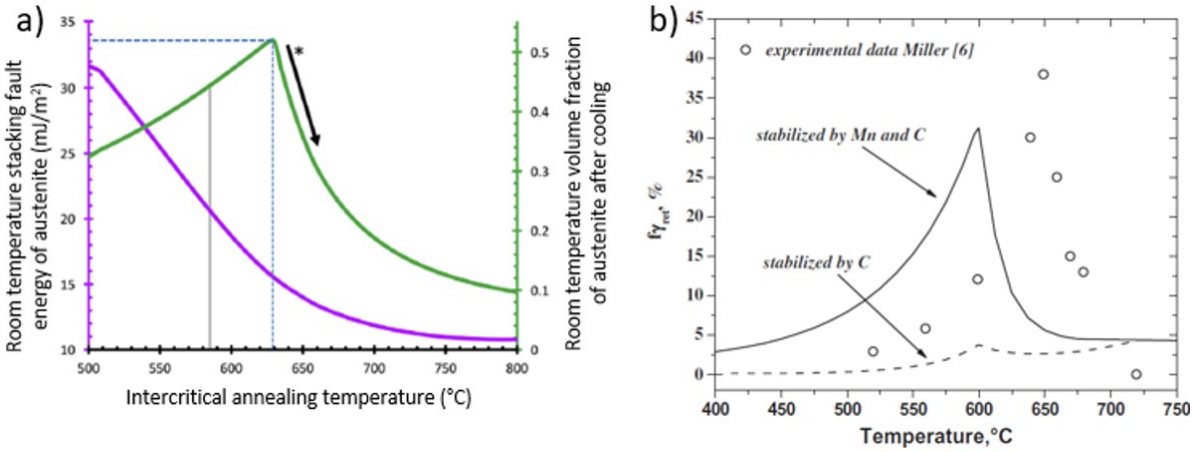

Figure 2.6: Modeling of the volume fraction of retained austenite at room temperature depending on the intercritical annealing temperature (1h) for steels of composition a) Fe-12Mn-3Al-0.05C (wt.%) [19] and b) Fe-5.7Mn-0.11C (wt.%) [21].

dissipates quicker than its manganese counterpart, and also that all the carbon atoms have partitioned in γ while around 2.5 Mn wt.% remain in α.[7]

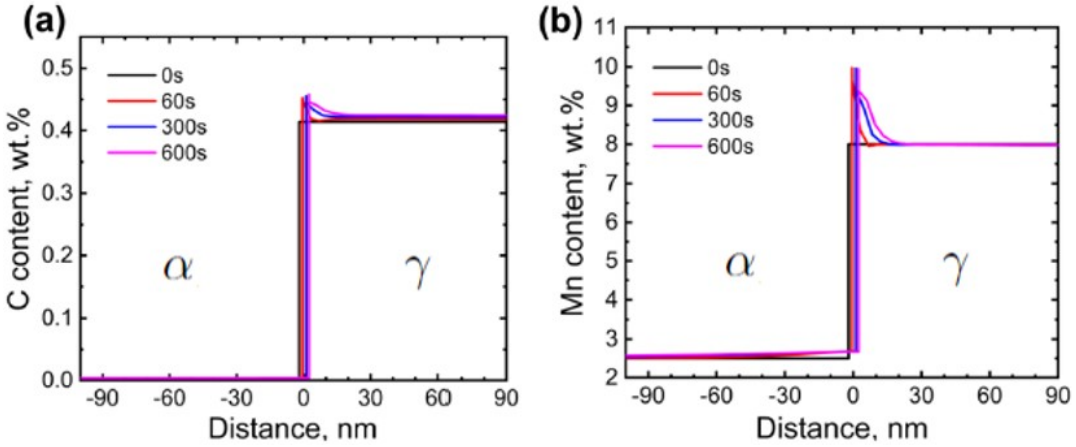

Figure 2.7: ThermoCalc simulation of a) carbon and b) manganese partitioning at the α/γ interface after annealing at 680°C for several holding times.[7]

The annealing time also impacts austenite stabilization. Benzing et al. have compared the volume fraction of retained austenite as well as the average retained austenite grain area for several annealing times at a fixed temperature (585°C) and for the same alloy (Fe-12Mn-3Al-0.05C wt%). The volume fraction of austenite has been measured by XRD and EBSD. The results of this experiment can be found in table 2.1. EBSD and XRD give similar results, and the retained austenite content as well as the average austenite grain area increase with the annealing time. Figure 2.8 allows the comparison of the EBSD maps taken after 0.5 hour of annealing and 8 hours of annealing. The difference is very visible, and shows that it is very difficult to detect retained austenite under 3% of volume fraction. It is very likely that no accurate measurement can be obtained under 0.5 hour of annealing for this alloy.[19]

2.3. Austenite stabilization through C-partitioning

Quenching and Partitioning (Q&P) steels are obtained through heat treatments similar to the one depicted in Figure 2.9. First, the steel is fully (γ) or partly ($\gamma + \alpha$) austenitized at high temperatures, then it is quenched at a quenching temperature QT between M_s and M_f to transform most of the austenite grains into martensite $\gamma - \alpha'$. After that, the alloy is held at the partitioning temperature PT above or equal to M_s to allow the carbon partitioning from the martensite to the untransformed austenite. This carbon enrichment of the austenite causes a decrease in the M_s and M_f temperatures of the alloy.

Annealing time (h)	Austenite content measured by XRD (%)	Austenite content measured by EBSD (%)	Average austenite grain area measured by EBSD (μm^2)
0	0	1	0.005
0.5	3	2	0.073
8	29	35	0.458
48	40	37	0.678

Table 2.1: Retained austenite volume fraction measured with XRD and EBSD, and austenite grain areas measured with EBSD at 585°C depending on annealing time[19]

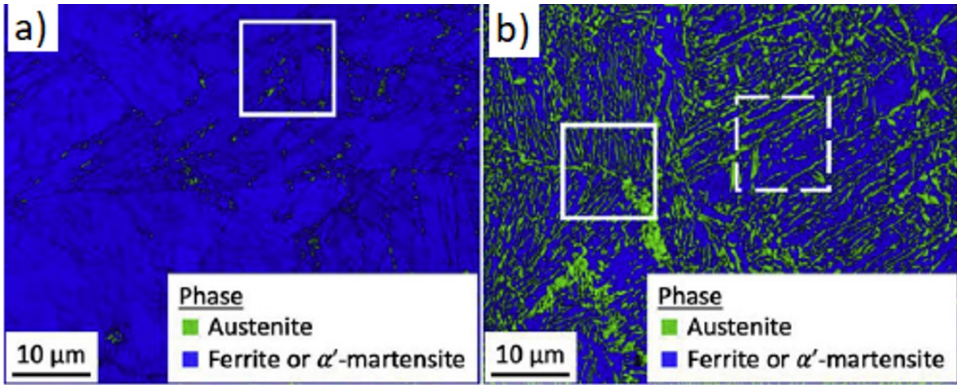

Figure 2.8: EBSD maps of ferrite and austenite phases at room temperature after a) 0.5 hour of annealing and b) 8 hours of annealing at 585°C.[19]

Finally, the steel is quenched to room temperature. Austenite grains with a sufficient concentration in carbon remain untransformed as RA, while the others transform into martensite. In the following, the main parameters influencing the volume fraction of retained austenite at the end of the Q&P heat treatment are discussed.[2][9][10]

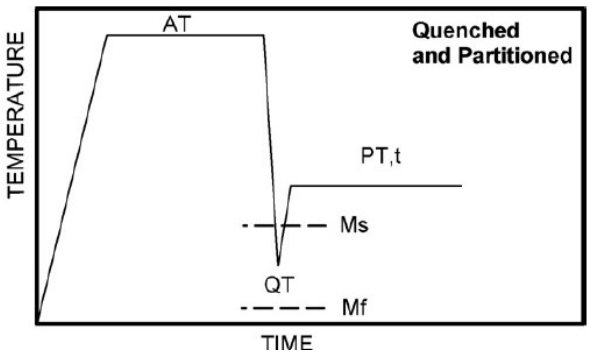

Figure 2.9: Schematic of the quench and partitioning process with AT the full or partial austenitization temperature, QT the quenching temperature, PT the partitioning temperature and t the partitioning time.[9]

The quenching temperature QT such that $M_f < QT < M_s$ directly impacts the volume fraction of martensite created after quenching. The relation between RA volume fraction at room temperature and QT is illustrated in Figure 2.10, and it shows that there is an optimum QT which results in the formation of the maximum RA volume fraction. Both simulation and experimental curves in Figure 2.10 were obtained for a Fe–0.60C–0.95Mn–1.96Si steel after partitioning for 10s at 500°C, and the optimum QT for this alloy is between 180°C and 185°C. When QT decreases below this optimum, the volume fraction of martensite formed upon quenching increases and thus the volume fraction of untransformed austenite that can stabilize into RA diminishes. When QT increases above this optimum, the volume fraction of untransfomed austenite increases. However, the carbon atoms of the reduced volume fraction of ferrite grains have to partition in a much higher number of untransformed austenite

grains. This results in slightly C-enriched untransformed austenite grains with low stability, most of which will transform into martensite during the final quench to room temperature. The volume fraction difference between simulation and experimental observed in figure 2.10 indicates that mechanisms other than carbon partitioning are taking place during the heat treatment.[2][9][10]

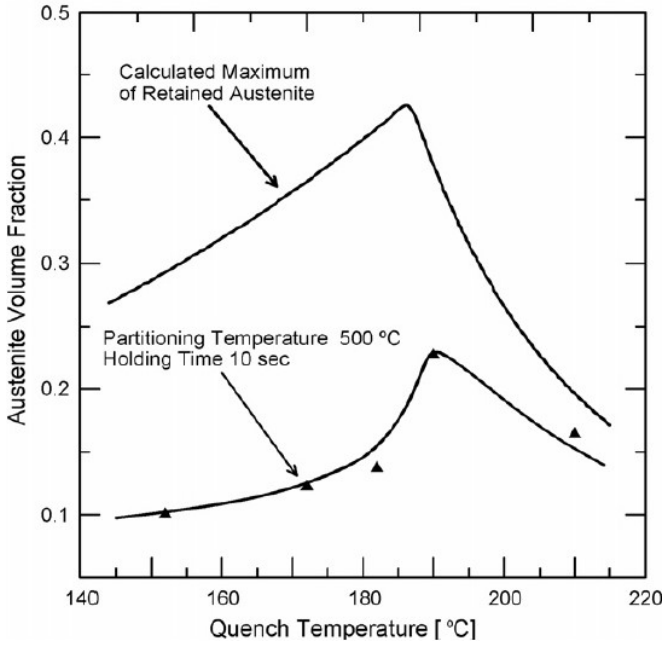

Figure 2.10: Volume fraction of retained austenite as a function of the quenching temperature in a Fe–0.6C–0.95Mn–1.96Si steel after partitioning for 10s at 500°C.[9]

The other important parameters which impact the RA volume fraction are the partitioning temperature PT and the partitioning time. For a relatively low PT, it is thermodynamically favorable for the carbon atoms to segregate and form transitional carbides rather than diffuse in austenite. However, a relatively higher PT might allow the formation of carbides, bainite and/or pearlite. Therefore, there exists an optimum PT for each alloy at each QT, as can be seen in Figure 2.11a for a Fe–0.60C–0.95Mn–1.96Si steel.[9][10]

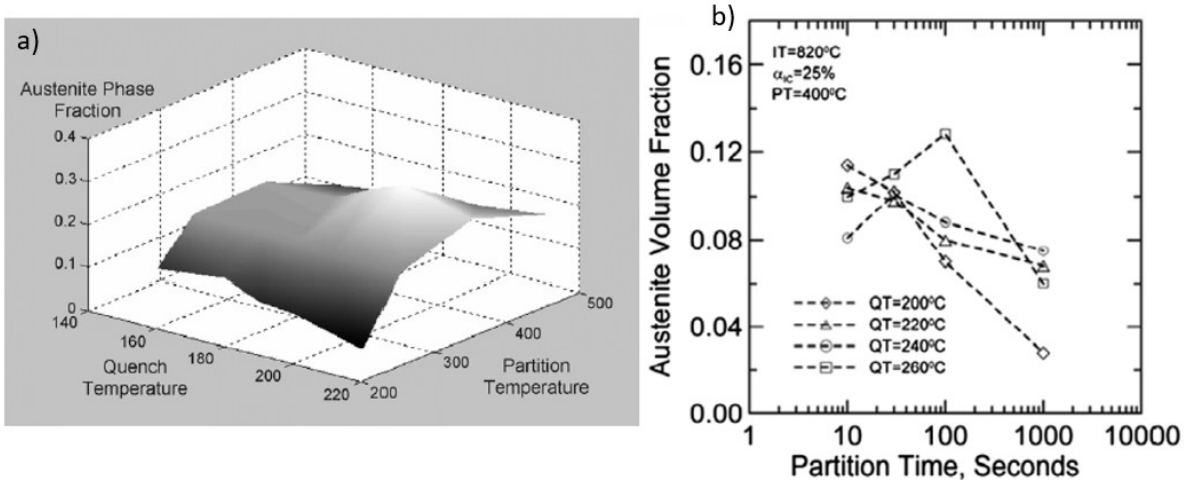

Figure 2.11: Variations of RA volume fraction in function of a) quenching and partitioning temperatures [9], and b) quenching temperature and partitioning time [10].

Partitioning time is also important as it affects the amount of carbon atoms that have partitioned in un-

transformed austenite grains, and thus whether they can stabilize into RA or not. Figure 2.11b shows the variations of RA volume fraction at room temperature depending on the partitioning time and the quenching temperature for a Fe-0.19C-1.59Mn-1.63Si-0.036Al (wt.%) steel. It can be seen that the maximum volume fraction of RA at room temperature is obtained for longer partitioning time when the quenching temperature increases. The decrease in RA volume fraction at longer partitioning times is partly due to carbide precipitation.[9][10]

2.4. Austenite stabilization through ferrite growth during intercritical annealing

Ferrite nucleation and growth is observed during the cooling of a fully austenitized steel to an intercritical temperature T_1. However, only ferrite growth takes place when cooling from T_1 to T_2, with $A_1 < T_2 < T_1 < A_3$, as the driving force for new nucleation is negligible. On the contrary, austenite growth in the intercritical region is obtained through heating from T_2 to T_1. Ferrite growth is a diffusion-based process and its kinetics are impacted by the partitioning of manganese and carbon at the austenite/ferrite interface. Depending on the temperature and the composition of the steel alloy, three separate mechanisms can be used to characterize ferrite growth. [22]

On one hand, paraequilibrium occurs when bulk diffusion of substitutional atoms is impossible while interstitial diffusion remains possible due to temperature contraints. The growth of ferrite is then solely dependent on the interstitial diffusion of small alloying elements (carbon), and the concentration of the other alloying elements stays constant. Figure 2.12(a) shows the phase diagram of Fe-Mn-C in paraequilibrium and in equilibrium at 780°C. The equilibrium diagram has dotted tie-lines linking the ferritic phase to the austenitic phase. For an alloy A belonging to the $\alpha + \gamma$ region, the manganese and carbon concentration of a γ grain can be read at the intersection between the tie-line of A and the separation line between the $\alpha + \gamma$ and γ regions. The concentrations of a α grain can be determined in a similar way. The tie-lines of the paraequilibrium phase diagram (red) are not drawn as they are all parallel to the carbon axis due to the absence of substitutional diffusion.[22]

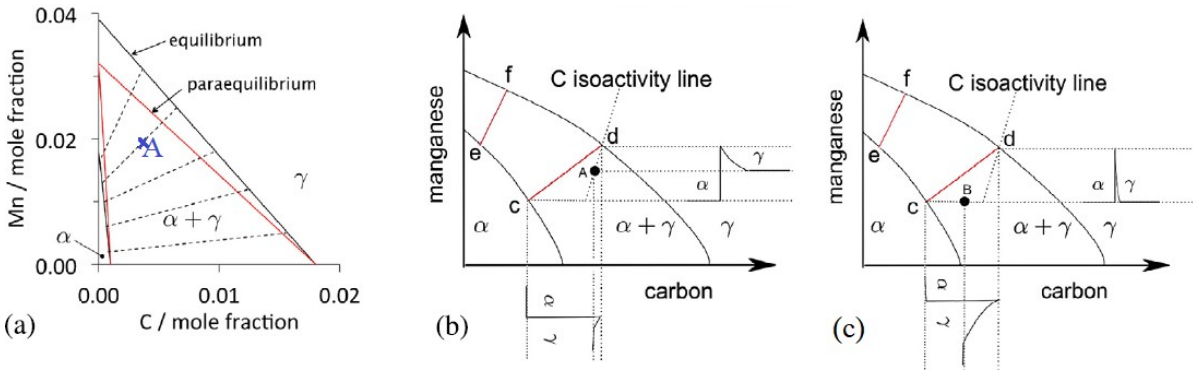

Figure 2.12: (a) Isothermal section of the Fe-Mn-C system at equilibrium and paraequilibrium at 780°C. Schematic isothermal sections of the Fe-Mn-C system (b) at partitioning local equilibrium and (c) at non-partitioning local equilibrium.[22]

On the other hand, there is a local equilibrium of alloying elements concentrations at the austenite-ferrite interface during cooling of a fully austenitized specimen. This local equilibrium must be preserved during ferrite growth, which results in all alloying element flux respecting equation 2.2.[22]

$$(c^{\gamma\alpha} - c^{\alpha\gamma})v = -D^{\gamma}\nabla c \tag{2.2}$$

The left term represents the rate at which solute is partitioned with $c^{\gamma\alpha}$ and $c^{\alpha\gamma}$ the elemental solubility of austenite and ferrite respectively, and v the velocity of the interface. The right term characterizes the diffusion flux from the interface, with D^{γ} the diffusion coefficient in austenite and ∇c the concentration gradient in the matrix. $c^{\gamma\alpha}$ and $c^{\alpha\gamma}$ are determined based on the phase diagram of the alloy for a fixed

temperature (isothermal reaction). $\bar{c}$ is called the far-field concentration and represents the concentration non affected by partitioning. In the case of a ternary steel alloy Fe-Mn-C, both manganese and carbon need to respect equation 2.2 simultaneously, which can be rewritten as equations 2.3.[22]

$$\begin{cases} (c_C^{\gamma\alpha} - c_C^{\alpha\gamma})v = -D_C^{\gamma}\nabla c_C \\ (c_{Mn}^{\gamma\alpha} - c_{Mn}^{\alpha\gamma})v = -D_{Mn}^{\gamma}\nabla c_{Mn} \end{cases} \tag{2.3}$$

Carbon diffuses very fast and interstitially while manganese diffuses at a slower pace and substitutionnaly. Therefore, $D_C^{\gamma} >> D_{Mn}^{\gamma}$ and no solutions of the system can be found for tie-lines intersecting ($\bar{c}_C$,$\bar{c}_{Mn}$). This means that the definition of how tie-lines are drawn must be adapted. The first possibility is to define $c_C^{\gamma\alpha} = \bar{c}_C$, as shown in Figure 2.12(b). In this case the gradient ∇c_C will become very small, reducing the driving force of carbon diffusion and effectively slowing it down. This ferrite growth mechanism is known as Partitioning Local Equilibrium (PLE), and is characterized by high manganese partitioning and diffusion in austenite (cf. Figure 2.13(b)). The second possibility is to define $c_{Mn}^{\alpha\gamma} = \bar{c}_{Mn}$ as illustrated in Figure 2.12(c). This time the manganese concentration gradient in austenite ∇c_{Mn} highly increases, creating a manganese spike at the α/γ interface but a very low diffusion in the austenite grain, as can be seen in Figure 2.13(c). This last ferrite growth mechanism is referred to as Non-Partitioning Local Equilibrium (NPLE). The phase transformation typically starts with PE conditions at the transformation's interfaces, then continues in NPLE conditions, and finishes in PLE conditions if enough time is provided.[22]

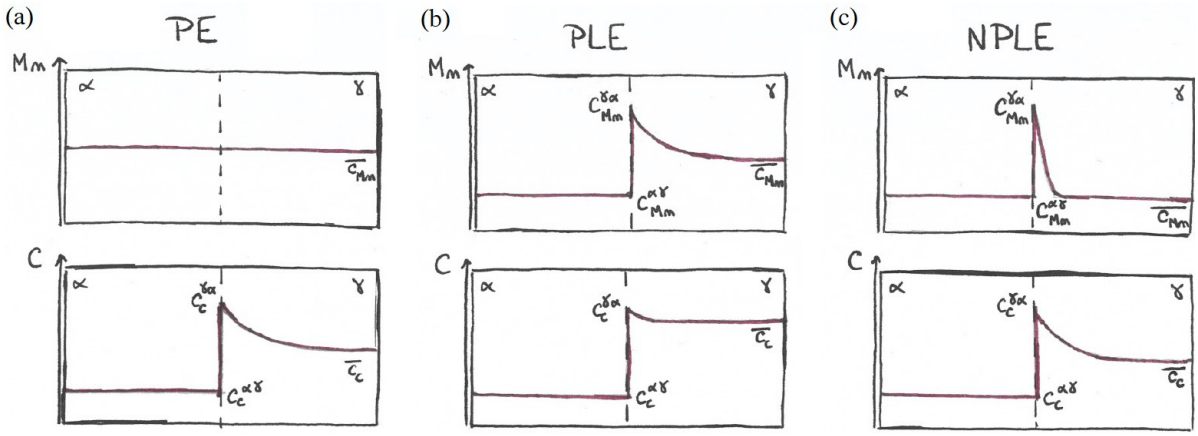

Figure 2.13: (a) PE, (b) PLE and (c) NPLE concentration profiles of manganese and carbon at the α/γ interface.[22]

2.5. Cyclic Phase Partial Transformation (CPPT)

Cyclic Partial Phase Transformation (CPPT) is a heat treatment in which the temperature is cycled at least three times between two extremes T_1 and T_2 belonging to the intercritical temperatures($A_1 < T_1 < T_2 < A_3$). Before the CPPT heat treatment starts, the alloy is commonly fully austenitized and then cooled and isothermally held at T_1. This allows the microstructure to be fully dual phased ferrite-austenite. The temperature is then cycled between T_1 and T_2 without any isothermal holding (Type I protocol, cf. Figure 2.14 (a)) or with isothermal holding (Type H protocol, cf. Figure 2.14 (b)). After a certain amount of cycles, the alloy is cooled down to room temperature [23]. To obtain a ferrite-martensite DP steel, the alloy has to be quenched from an intercritical temperature.

The CPPT heat treatment was originally designed to distinguish the nucleation and growth phenomena. After the first isothermal holding at T_1, only α and γ grains are present in the microstructure. By cycling between T_1 and T_2 in the intercritical region, no phase transformations occur and the driving force for new nucleation is negligible. This permits to neglect the nucleation of new grains. Austenite grains are characterized by a FCC lattice, and ferrite grains by a BCC lattice. The volume per atom in an FCC lattice is inferior to the volume per atom in a BCC lattice. Therefore the growth of the austenite grains γ is characterized by a decrease in the total length of the specimen. In the same way, the growth of the

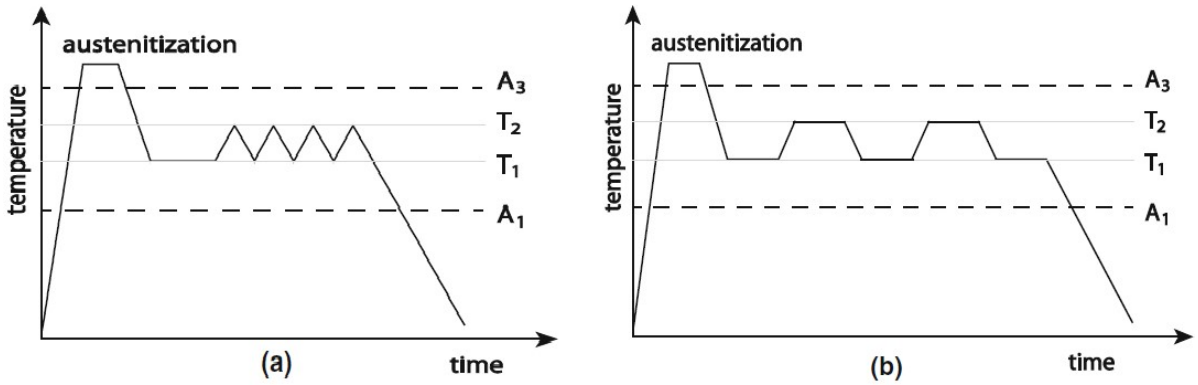

Figure 2.14: Examples of temperature programmes for types (a) I and (b) H of cyclic experiments[23]

ferrite grains α is reflected by an increase in the length of the sample. These changes of length can be observed through dilatometry experiments. The expected behaviour would then be a direct relationship between the length change and the temperature, from the time that the intercritical region has been reached, and thus would be relatively easy to predict and control. However, the real behaviour is very different, as shown in Figure 2.15.[23]

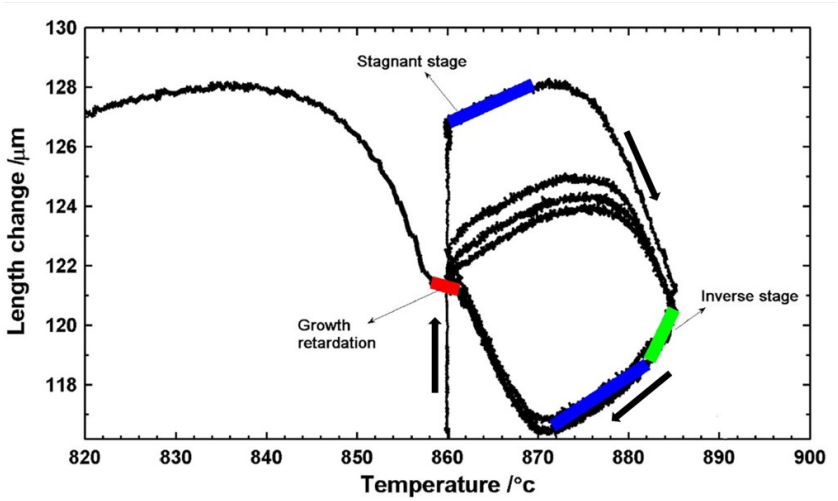

Figure 2.15: Dilatometry measurement during a type I CPPT experiment[23]

To obtain Figure 2.15, a type I CPPT experiment between $T_1 = 860$°C and $T_2 = 885$°C, and a simultaneous dilatometry measurement have been realised in a Fe-0.023C-0.17Mn (wt.%) alloy. The sample has been previously austenitized and the dilatometry measurement is shown when the temperature first reached T_1. The sample has then been held at T_1 for a relatively long time to allow the formation and growth of ferrite, which is why the first cycle shows a higher length change than the following cycles with no holding. The black arrows indicate the time component. Three non-expected growth behaviours have been identified thanks to CPPT: the stagnant stage, the inverse stage and the growth retardation.

• The stagnant stage reports none or a very small phase transformation for a big temperature difference, and is shown in blue in Figure 2.15. It happens at the beginning of the cooling or heating process, and reflects the transformation interfaces not moving even when provided by sufficient driving force.[23]
• This stage is followed by a direct transformation stage, in which the length change is directly related to the growth of γ or α, respectively due to heating or cooling.[23]
• After that, the transformation takes place in the opposite direction from the imposed temperature change during the inverse stage (in green). This means that γ grows while cooling or that α grows

while heating. The inverse stage is not found in type H CPPT as enough time is given to the material to accomodate to the change of temperature.[23]
• Finally the growth retardation (in red) is a temporarily slowed down $\gamma \rightarrow \alpha$ transformation happening at the end of the last cycle.[23]

2.5.1. Current applications

CPPT heat treatments have been used in three main research questions:

i) Studying the interfacial segregation of alloying elements. The influence of alloying elements such as manganese on the kinetics of phase transformation can be studied through CPPT. Figure 2.16 shows two dilatometry measurements of CPPT experiments for (a) Fe-0.1C-0.5Mn (wt.%) and (b) Fe-0.1C-1.0Mn (wt.%). The T_1 and T_2 temperatures are different in those experiments as the composition of an alloy determines its intercritical region. The stagnant stage and the growth retardation stage are getting longer with an increase in manganese concentration. This means that the increase in manganese concentration leads to an increasing delay of both the $\alpha \rightarrow \gamma$ and $\gamma \rightarrow \alpha$ transformations. It has been found that the difference between the interface velocity and the manganese diffusion rate in γ causes the formation of a manganese peak at the interface. This peak is responsible for the delayed start of the stagnant stage and the growth retardation as it slows down the migration of the transformation interfaces.[23][24]

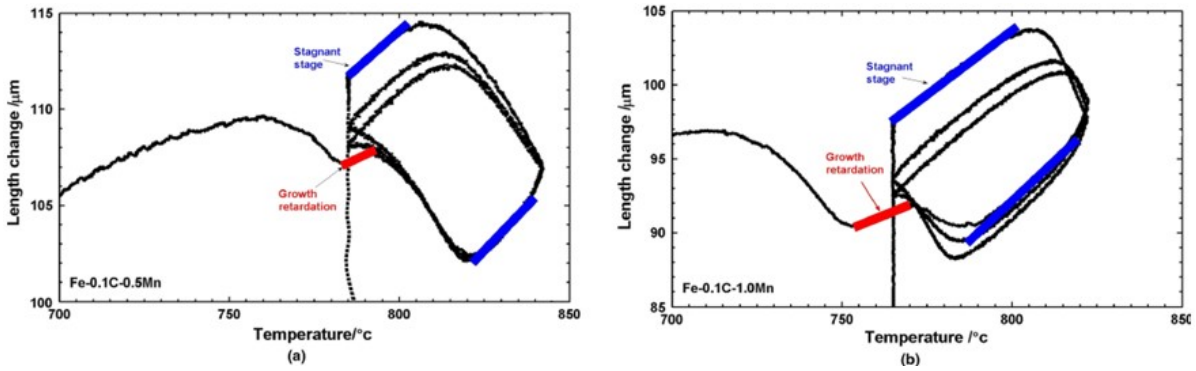

Figure 2.16: Comparison of dilatometry results from CPPT experiments with (a) Fe-0.1C-0.5Mn (wt.%) and (b) Fe-0.1C-1.0Mn (wt.%).[23]

ii) Measuring interface mobility. It has been proven that interface mobility is not only impacted by the alloying elements, but also by the direction of the phase transformation. Figure 2.17 shows the evolution of the effective mobilities depending on the composition of the alloy, the temperature and the phase transformation. It can be seen that the effective mobilities of the $\gamma \rightarrow \alpha$ and $\alpha \rightarrow \gamma$ transformations increase and decrease respectively with an increase in temperature.[25]–[28] Experimental data for interface mobility is very difficult to obtain [25], and the effective mobility values in Figure 2.17 were calculated through model fitting based on the LE and NPLE models. The preliminary data was obtained through DICTRA simulations of CPPT experiments. It can be seen again that an increase in the mass fraction of manganese slows down the γ-to-α effective mobility, which is due to the low kinetics of ferrite formation. [26]

iii) Controlling microstructure. It is also possible to control the microstructure of an alloy through CPPT due to the Mn-partitioning and ferrite growth mechanisms. When a Fe-C-Mn DP steel is heated up from room temperature to T_1, and then intercritically annealed at T_1, the manganese and carbon partition from α to γ, creating a concentration spike of Mn and C in γ at the $\alpha - \gamma$ interface. As shown in Figure 2.18a, this spike is accompanied by a depletion peak on the α side of the $\alpha - \gamma$ interface. During CPPT, the temperature is cycled between T_1 and T_2. As the temperature increases, the austenite grains are growing onto the ferrite grains, which moves the position of the α/γ interface. The interface mobility is faster than the substitutional diffusion of Mn, therefore an Mn spike is formed in γ next to the new

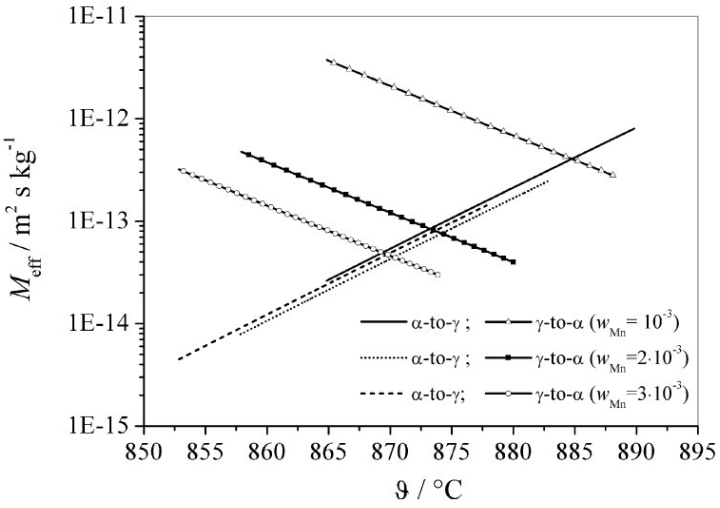

Figure 2.17: Effective mobilities based on composition, temperature and phase transformation, with W_{Mn} the mass fraction of manganese.[26]

α/γ interface, while the previous spike is only attenuated and does not disappear. This phenomenon is illustrated on Figure 2.18b.[29]

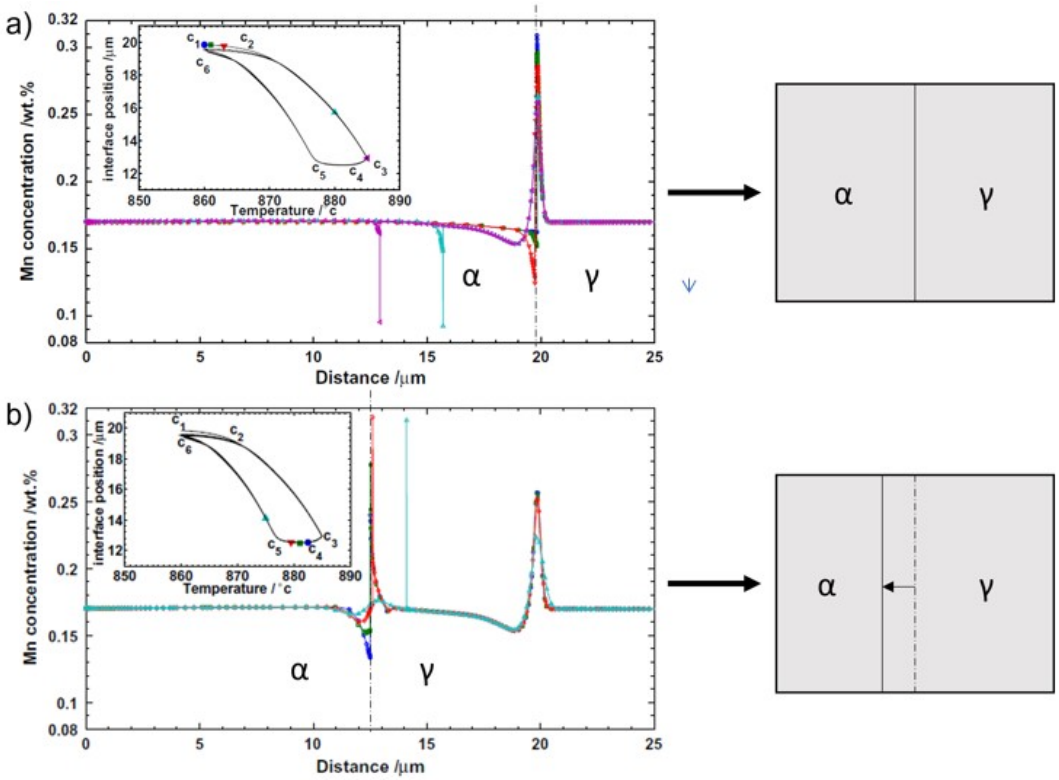

Figure 2.18: Modeling of the evolution of the Mn profile during type I CPPT and comparison with the associated interface position curve for a Fe–0.17Mn–0.023C (wt.%) steel a) at T_1 and b) at T_2.[29]

Faharani et al. exploited this phenomenon successfully to prevent band-formation in a medium Mn-steel through controlled and local Mn enrichment at austenite-ferrite interfaces. The repeated change in temperature of the CPPT makes the $\alpha - \gamma$ interface move back and forth, creating an Mn enriched zone instead of a single spike. This resulted in the formation of pearlite rims around low Mn ferrite grains, in the locally Mn-enriched zone at the interface (cf. Figure 2.19).[11]

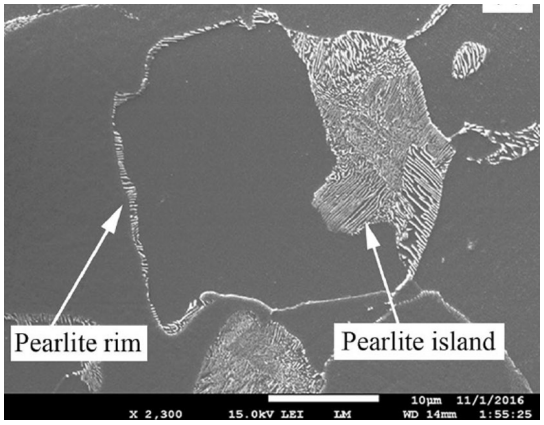

Figure 2.19: SEM micrograph after type H CPPT experiment showing ferrite grain pearlite rim in a low Mn region.[11]

2.5.2. On the application of CPPT to stabilize austenite in DP steels

CPPT heat treatments have been successful in controlling microstructure by taking advantage of the partitioning mechanism, and could be used towards the interfacial stabilization of austenite in medium Mn DP steels. However, there are several challenges complicating this application.

i) Low kinetics of ferrite formation and growth: As previously explained in section 2.4, the kinetics of ferrite growth can proceed under three thermodynamics modes of PE, NPLE and PLE at the transformation interfaces. It has been found that NPLE conditions can best explain the transformation stages in a CPPT experiment.[22][30]

Figures 2.20a and b show the leading ferrite and austenite formation mechanisms in the intercritical region respectively, at T=660°C and depending on Mn and C concentrations. The $\gamma \rightarrow \alpha$ transformation starts mainly in the PLE mode for medium Mn steels (cf. Figure 2.20a). Hence, a CPPT experiment at intercritical temperatures in a DP steel starting from full austenitization will have very slow kinetics of ferrite growth. Figure 2.20b indicates that the $\alpha \rightarrow \gamma$ transformation for medium Mn steels begins almost exclusively in the NPLE mode. This means that the $\alpha \rightarrow \gamma$ transformation has faster kinetics than the $\gamma \rightarrow \alpha$ transformation.[30] Therefore, the most efficient way to obtain an $\alpha - \gamma$ microstructure in a medium Mn steel at isothermal intercritical holding is to take advantage of the NPLE fast kinetics by heating the steel up from room temperature to T_1 or T_2.

ii) Obtention of a sufficient Mn concentration: To obtain a DP steel, the alloy must be quenched from an intercritical temperature. The austenite grains would typically transform into martensite while the ferrite grains remain stable. To ensure the stabilization of retained austenite during quenching, austenite grains must have sufficient Mn and C concentrations, which can be calculated from the martensite start temperature formula. Equation 2.4 has been established for a Fe-C-Mn-Al-Si TRIP alloy [20], and has successfully modelled the Ms dependency on composition for Fe-Mn-C alloys[21].

$$M_S = 539 - 423C - 30.4Mn - 7.5Si + 30Al \tag{2.4}$$

Figure 2.21 shows the evolution of Ms in function of Mn concentration based on equation 2.4, for a fixed carbon weight percentage of 0.2wt.%. It can be seen that to avoid martensite formation after quenching at room temperature (25°C), a Mn concentration of 14.13 wt.% is needed (green dot). As a precaution, the target temperature will be set at -10°C, which corresponds to 15.30wt.% manganese (red dot). Furthermore, the manganese spike created through partitioning is located on a very thin area at the austenite-ferrite interface. Through CPPT and the migration of the interface, the enriched region should become wider but with a lowered concentration. Therefore, to chemically stabilize austenite the Mn concentration after CPPT and attenuation of the enriched area should be higher than 15.30wt.%. Due to the partitioning and diffusion mechanisms of C in γ, the C concentration in γ will be higher than the initial 0.2 wt.%, which leads to a homogeneous C-enrichment of γ.

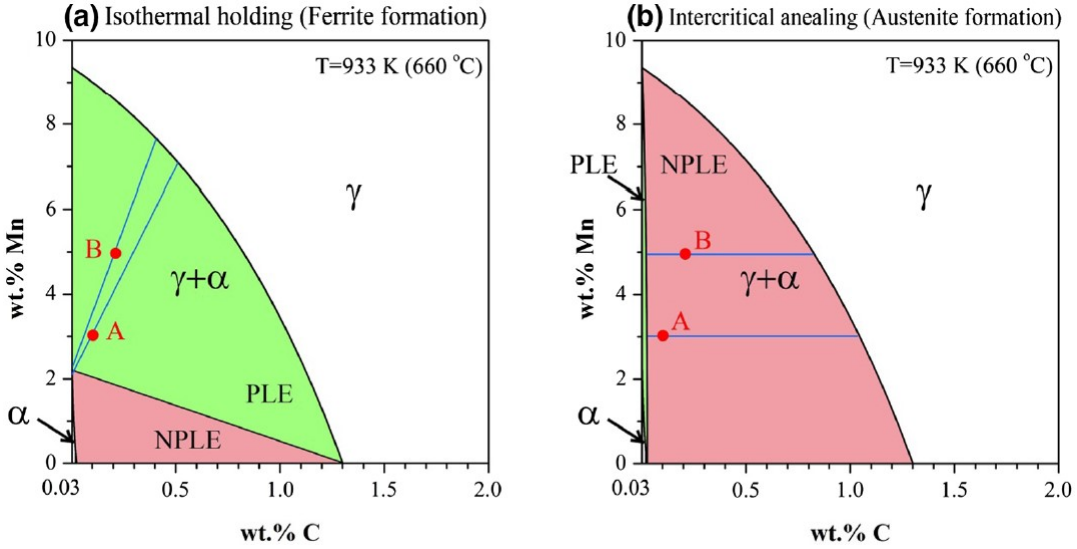

Figure 2.20: Isothermal section of an equilibrium phase diagram for (a) ferrite growth and (b) austenite growth in a Fe-Mn-C steel at T=660°C[30]

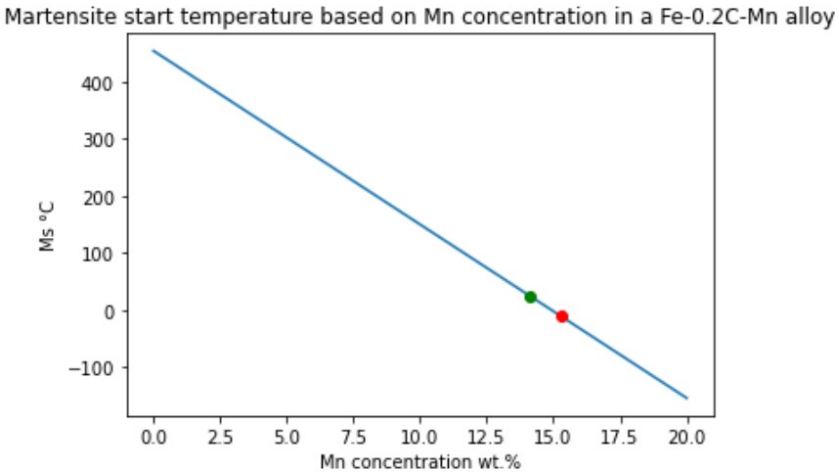

Figure 2.21: M_s based on Mn concentration in a Fe-0.2C-Mn (wt.%) DP steels, based on equation 2.4.

If these conditions are reunited, then the austenite phase should be stabilized at room temperature. Figure 2.22 represents a possible CPPT heat treatment and the expected microstructure at each stage. The austenite (1) and ferrite (2) grains should alternatively grow at the temperatures T_2 and T_1 respectively. A DP steel is created through quenching from the intercritical region, which means from a temperature T such that $T \in [A_1, A_3]$. The conclusive microstructure should be similar to a common DP steel (4), but some martensite grains should be surrounded by a shell of retained austenite (3).

iii) Detection of RA: In optical microscopy, a retained austenite grain is almost undistinguishable from a martensite grain [15]. If the stabilization of austenite as a shell around some martensite grains is successful, then its shape can allow its identification in optical microscopy (upon a sufficient resolution). A similar shape of pearlite has been successfully created with a thickness of around 3μm. Thinner grains would be difficult to even detect [11]. The same issue appears in SEM, but EDS might be useful to detect manganese gradients and once again the shape of the grains can be helpful for identification. The best results have been found through XRD and EBSD, with an accurate detection down to a retained austenite volume fraction of 3%.[19]

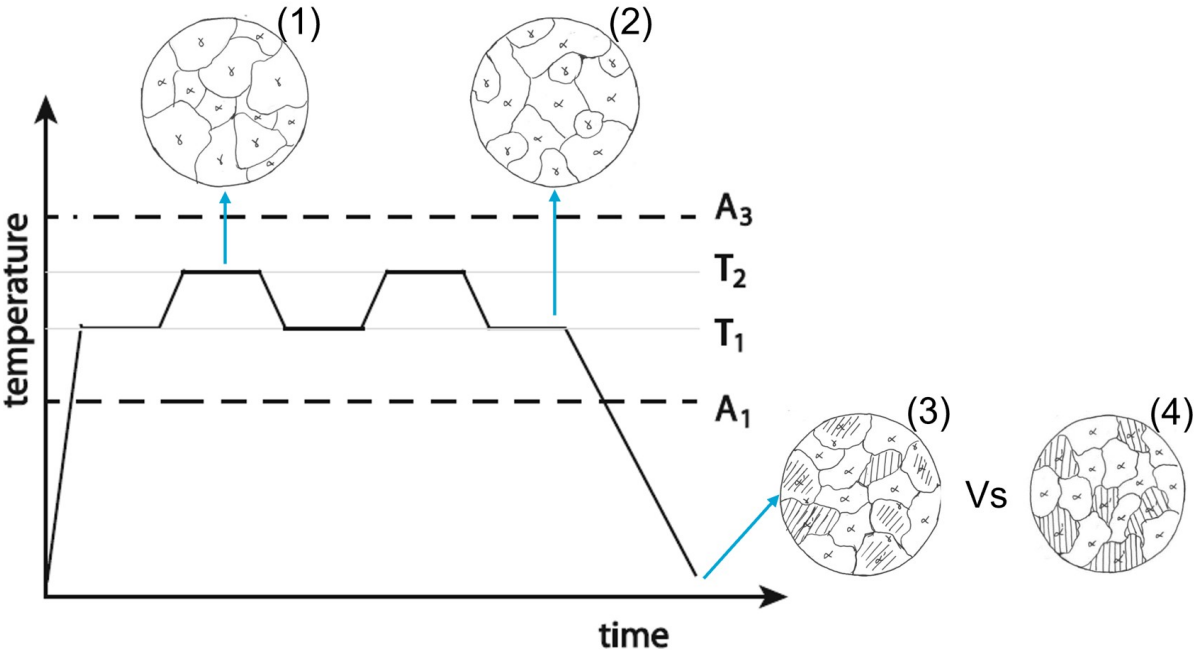

Figure 2.22: Prediction of the evolution of the microstructure of a DP steel during a CPPT heat treatment.

3

Modelling and experiments

3.1. Sample selection

Four steel alloys were selected for this investigation, the chemical compositions of which are gathered in Table 3.1. 2Mn, 4Mn and 6Mn have similar compositions apart from their Mn concentrations. The reason behind their selection is to observe the differences in the Mn-enrichment happening at the α/γ interface based on the initial Mn concentration. 6MnNi is present to obtain an insight on the influence of Ni over the stabilization of austenite at room temperature.

Name	Alloy	Fe (wt.%)	Mn (wt.%)	C (wt.%)	Si (wt.%)	Ni (wt.%)
2Mn	2926A	96.4	2	0.2	1.5	0
4Mn	2926B	94.4	3.8	0.19	1.4	0
6Mn	2926C	92.4	5.8	0.19	1.4	0
6MnNi	2926D	90.9	5.7	0.19	1.4	1.6

Table 3.1: Chemical compositions of the samples.

3.2. ThermoCalc modelling

The ThermoCalc software was used to obtain the phase diagrams of each sample. The DICTRA function of ThermoCalc coupled to the TCFE12 and MOBFE7 databases was used to simulate the partitioning and diffusion of manganese at the α/γ interface. Austenite to ferrite transformations were simulated in a 1D geometry with a starting austenite grain size of 25μm. The formation of ferrite grains was allowed on the left interface from a driving force of 1E-5J. For simulations starting at room temperature, a ferrite grain of 25μm was used as the initial state. The formation of austenite grains was allowed on the left interface from a driving force of 1E-5J. A planar interface between austenite and ferrite is assumed.

3.3. Heat treatments and characterization

All heat treatments were performed on 10x4x3mm (+/- 0.05mm) samples using a Bähr DIL 805A/D/T quenching dilatometer. The dilatation of the specimens was measured in the longitudinal direction. All experiments were done in vacuum with a pressure of 2.$10^{-}4$ mbar, apart from quenchs which were assisted by helium. All CPPT samples were first heated with a rate of 10°C/s at 950°C and held for 5mins to reach full austenitization, then they were subjected to different CPPT routes.

After having been heat treated, all samples were cut in the transverse direction, sanded with SiC paper, polished until a 1μm grain, and then etched with a 2 pct Nital etchant for 10secs. Their microstructures were subsequently evaluated using a table-top JSM-IT100 Scanning Electron Microscope (SEM). Energy Dispersive Spectroscopy (EDS) was performed to evaluate the partitioning of Mn in the resulting

microstructure. The volume fraction of retained austenite was determined through X-Ray Diffraction (XRD) using a Bruker D8 Advance diffractometer on non-etched samples. Samples were then polished for 10 mins with OPS diamond suspension to allow for an Electron Back-Scattered Diffraction (EBSD) analysis. EBSD measurements were acquired using a Helios G4 PFIB UXe with a step-size of 50nm to determine the volume fraction and shape of the RA grains.

4

Design of CPPT heat treatments

The four selected samples have different chemical compositions, therefore adequate CPPT heat treatments must be designed for each of them. The first step of the design is to determine appropriate T_1 and T_2 temperatures for each sample. To do so, both modelling and experimental means were used. The most adequate route is then be determined experimentally.

4.1. Determination of the temperatures

As previously explained in section 2.5, the principle of CPPT is to isolate the growth mechanisms of the austenite and ferrite grains by cycling between two intercritical temperatures T_1 and T_2, such that $T_1 < T_2$. The range of intercritical temperatures is comprised between Ac_1 and Ac_3 when heating from room temperature, and Ar_1 and Ar_3 when cooling from a full austenitization state.

4.1.1. Through modelling

By modelling phase diagrams through ThermoCalc, it is possible to determine the equilibrium intercritical temperatures Ae_1 and Ae_3 for each sample. They do not take into account the variations brought by cooling and heating, but constitute a good first approximation. Figure 4.1 shows two phase diagrams. The diagram on the left varies in temperature and Mn concentration (wt.%) only, thus the temperatures of the samples 2Mn, 4Mn and 6Mn can be found. The diagram on the right shows variations in temperature and Ni concentration (wt.%), and can be used for the temperatures of samples 6Mn and 6MnNi. The Ae_1 and Ae_3 temperatures determined through modelling are gathered in Table 4.1.

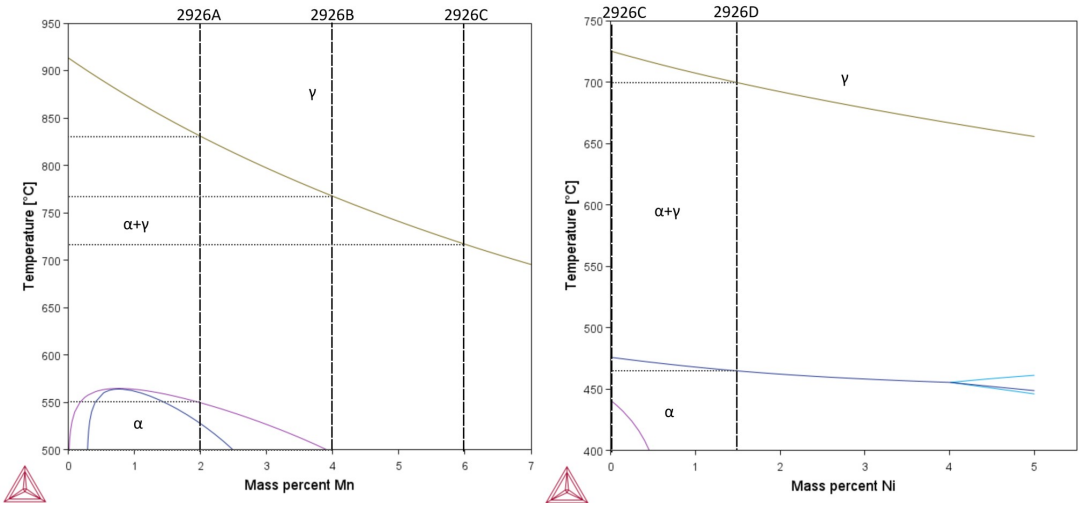

Figure 4.1: Phase diagrams of the 2Mn, 4Mn, 6Mn and 6MnNi samples computed through ThermoCalc

Sample	Ae_1	Ae_3
2Mn	550°C	835°C
4Mn	500°C	770°C
6Mn	475°C	720°C
6MnNi	460°C	700°C

Table 4.1: Equilibrium intercritical temperatures extracted from the phase diagrams of Figure 4.1

It is interesting to note that the temperature gap between Ae_1 and Ae_3 decreases when the Mn concentration increases. The Ae_3 and Ae_1 temperatures found also decrease with Mn concentration, which seems right as Mn is an austenite stabilizer element. However, the Ae_1 temperatures are very low and most probably not reliable.

4.1.2. Through experiments

To determine the limits of the intercritical range during heating (Ac_1 and Ac_3) and during cooling (Ar_1 and Ar_3), each sample was submitted to the heat treatment shown in Figure 4.2. During this heat treatment, all cooling and heating apart from quenchs were made with a rate of 10°C/s. As the samples have an unknown initial microstructure, they are first heated up to an annealing temperature of 950°C for 5mins to obtain a fully austenitic microstructure. This temperature was chosen based on the equilibrium temperatures found through modelling, as it is at least 125°C higher than the Ae_3 of each sample, and therefore should be above the intercritical range despite the possible approximation mistakes. By cooling the sample, the $\gamma - \alpha$ transformation will begin when Ar_3 is reached and finish at Ar_1. This transformation can be monitored through dilatometry as the lattice parameter of a BCC crystal (ferrite) is bigger than for a FCC crystal (austenite). The second cycle of this heat treatment has for aim to obtain a known microstructure at room temperature. From there, the third cycle can be used to determine the Ac_1 and Ac_3 temperatures of samples with a full martensitic microstruture.

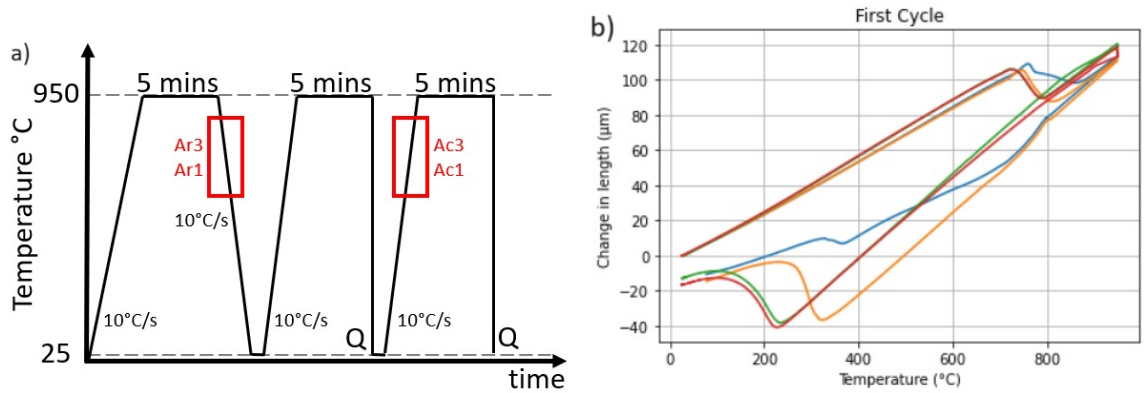

Figure 4.2: a) Heat treatment designed to determine the intercritical range of temperatures of each sample. b)Dilatometry measurements for the first cycle of the heat treatment on 2Mn, 4Mn, 6Mn and 6MnNi.

Figure 4.2b shows the dilatometry curves obtained for all samples for the first cycle of the heat treatment of Figure 4.2a. It can be noticed that none of the curves are showing the length variation characteristic of the formation of ferrite. This was expected for 6Mn and 6MnNi, as their high concentration in Mn (6wt.%) leads to very low ferrite formation kinetics. However, the dilatometry curves of 2Mn and 4Mn, with respectively 2wt.% Mn and 4wt.% Mn, were expected to show the formation of ferrite.

The dilatometry curves of all the samples during the third cycle of the heat treatment are showing changes in length characterizing the intercritical region (cf. Figure 4.3), which allows the determination of the Ac_1 and Ac_3 temperatures for each sample. From these, the T_1 and T_2 temperatures for the CPPT can be selected. The Ac_1, Ac_3, T_1 and T_2 temperatures are gathered in Table 4.2.

The trial CPPT heat treatments realized with the temperatures of table 4.2 resulted in fully martensitic microstructures for 4Mn, 6Mn and 6MnNi. This means that the temperatures used were too high, even

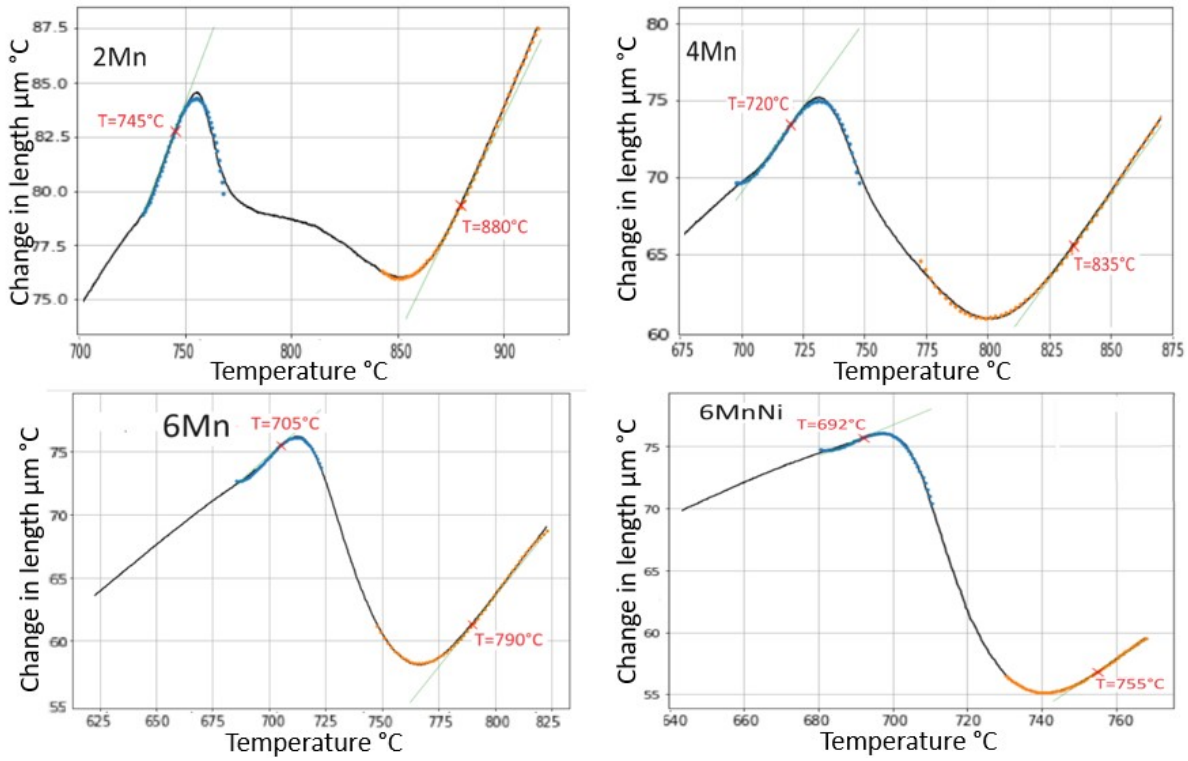

Figure 4.3: Dilatometry measurements for the third cycle of the heat treatment on 2Mn, 4Mn, 6Mn and 6MnNi : Ac_1 and Ac_3

Sample	Ac_1	Ac_3	T_1	T_2
2Mn	750.7°C	873.5°C	770°C	860°C
4Mn	725.4°C	825.5°C	745°C	815°C
6Mn	706.8°C	767.4°C	726°C	757°C
6MnNi	701.5°C	750.4°C	721°C	740°C

Table 4.2: Ac_1 and Ac_3 temperatures of 2Mn, 4Mn, 6Mn and 6MnNi based on Figure 4.3

though the dilatometry curves do show small amounts of ferrite formation. An example of the resulting microstructure for a 4Mn sample after cyclic annealing between $T_1 = 745°C$ and $T_2 = 815°C$ can be seen in Figure 4.4.

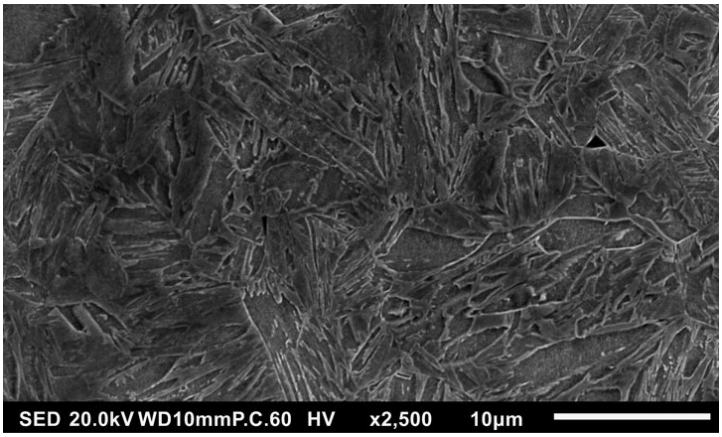

Figure 4.4: SEM micrograph of 4Mn after a CPPT treatment between $T_1 = 745°C$ and $T_2 = 815°C$.

The most probable reasons behind the errors regarding the temperatures are the slow kinetics of ferrite

growth. The heat treatment of Figure 4.2 has cooling and heating rates of 10°C/s, which might be too fast to register ferrite formation through Ar_1 and Ar_3, and might also increase the perceived Ac_1 and Ac_3. Therefore, slow cooling and slow heating experiments with a rate of 0.1°C/s should enable the accurate determination of the intercritical region's limits. Slow heating experiments are preceded by a full austenitization of the sample at 950°C for 5 mins and a quench. This way, the slow heating experiments have a fully martensitic starting microstructure.
As can be seen in Figure 4.5, the slow heating of 6Mn results in Ac_1 and Ac_3 temperatures with around 50°C of difference compared to the ones found with the previous experiment. The determination of the Ac_1 and Ac_3 temperatures of 6MnNi through a slow heating dilatometry experiment (cf. Figure 4.5) isn't very reliable as cementite seems to form at similar temperatures as ferrite. The Ar_1 and Ar_3 temperatures are still not possible to find through slow cooling dilatometry curves for 4Mn, and therefore slow cooling experiments were not performed on 6Mn and 6MnNi. The resulting Ac_1 and Ac_3 temperatures for 4Mn, 6Mn and 6MnNi as well as the Ar_1 and Ar_3 temepartures for 2Mn are gathered in Table 4.3.

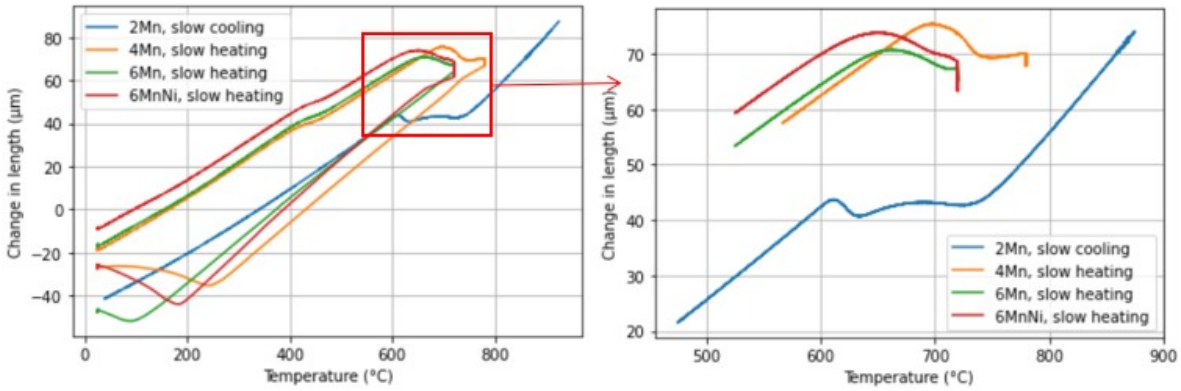

Figure 4.5: Dilatometry curves of a slow cooling treatment on 2Mn and slow heating treatments on 4Mn, 6Mn and 6MnNi

Sample	Ac_1	Ac_3	Ar_1	Ar_3
2Mn	−−	−−	630°C	750°C
4Mn	700°C	750°C	−−	−−
6Mn	660°C	715°C	−−	−−
6MnNi	660°C	715°C	−−	−−

Table 4.3: Ac_1, Ac_3, Ar_1 and Ar_3 temperatures of 2Mn, 4Mn, 6Mn and 6MnNi based on slow cooling/heating experiments

While the Ae_1 temperatures obtained through modelling are very different from the Ac_1 temperatures found during slow heating, the Ae_3 and Ac_3 temperatures are quite similar.

4.2. Determination of the route

A total of three CPPT's routes were chosen to be compared, as illustrated by Figures 4.6a, 4.6b and 4.6c. All the routes start with a full austenitization at 950°C for 5mins. Each cycle consists of an isothermal intercritical annealing of 20 mins. As this research is done towards an industrial application, the duration of each cycle must stay relatively short. Moreover, the first dilatometry experiments have shown that it is sufficient to allow ferrite to form despite its low kinetics. This can be seen in Figure 4.6d, with cycles 1 and 3 showing a decrease in length associated to austenite formation, and cycles 2 and 4 showing an increase in length characterizing ferrite formation. A plateau in ferrite formation happens after 20 mins of annealing in cycles 2 and 4. Therefore, longer annealing times should not impact the final microstructure of the treated DP steels.

From the slow cooling/heating experiments made to determine the transition temperatures, it has been found that the kinetics of ferrite formation are too low to be able to observe ferrite growth by cooling from a full austenitization state in a short time for samples with 4wt.%Mn or more. Routes 1 and 2, re-

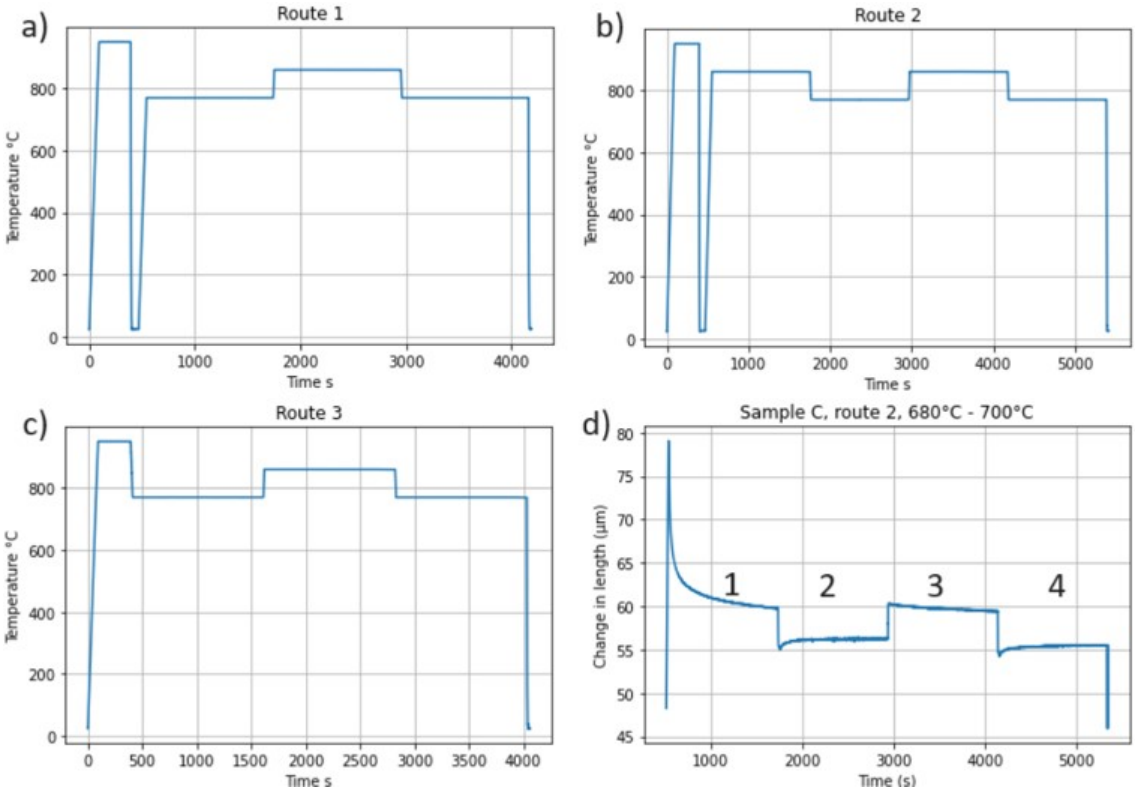

Figure 4.6: a, b and c) Schematics of the three main possible CPPT routes and d) dilatometry curve of a CPPT treatment on 6Mn following route 2 with $T_1 = 680°C$ and $T_2 = 700°C$

spectively Figure 4.6a and b, aim to take advantage of the higher kinetics of austenite formation due to the NPLE model by heating the sample from a fully martensitic state at room temperature to T_1 and T_2 respectively. Route 3 however, directly cools down to T_1 from the full austenitization state. In this case, ferrite formation can be observed for samples with a relatively low manganese concentration such as 2Mn. These different routes result in different starting microstructures, with a fully martensitic steel in route 1 and 2 and with a fully austenitic steel in route 3. The samples were cut from cold-rolled sheets with a thickness of 3mm. As the duration of the full austenitization in each of the routes is very short (5 mins), it is expected for bandformation to happen, especially in 6Mn and 6MnNi which both contain 6wt.% of Mn.

To obtain a $\alpha/RA/\alpha'$ microstructure, it is necessary for the last cycle of the CPPT heat treatment to be at T_1. After the first annealing cycle, the manganese atoms inside the ferrite grain have partitioned towards the austenite grain, and a concentration spike of Mn has formed on the austenite side of the α/γ grain boundary. If the sample is then heated up, the α/γ interface will move towards the ferrite grain. As the interface moves faster than the Mn atoms diffuses in austenite, the Mn spike will remain inside the austenite grain and will slowly widen and decrease in concentration. At the same time, a new spike will be formed at the new position of the α/γ interface, as shown in Figure 4.7b. After being quenched, the microstructure obtained at room temperature is expected to be $\alpha/\alpha'/RA/\alpha'$. However, if the sample is cooled down to T_1 during the last CPPT cycle, then the α/γ interface moves towards the austenite grain. The Mn spike moves simultaneously to the grain boundary and a widened peak forms at the austenite side of the α/γ interface. After quenching, the expected microstructure obtained should contain interfacial RA as illustrated by Figure 4.7a.

Figure 4.8 shows the dilatometry curves obtained through routes 1 and 2 for 6Mn, with $T_1 = 726°C$ and $T_2 = 757°C$. Both routes have similar changes of length during each cycle. Therefore, starting the cycles at a lower temperature T_1 do not increase the distance travelled by the α/γ interface compared to starting at a higher temperature T_2. This means that the two first cycles of route 1 only serve to form

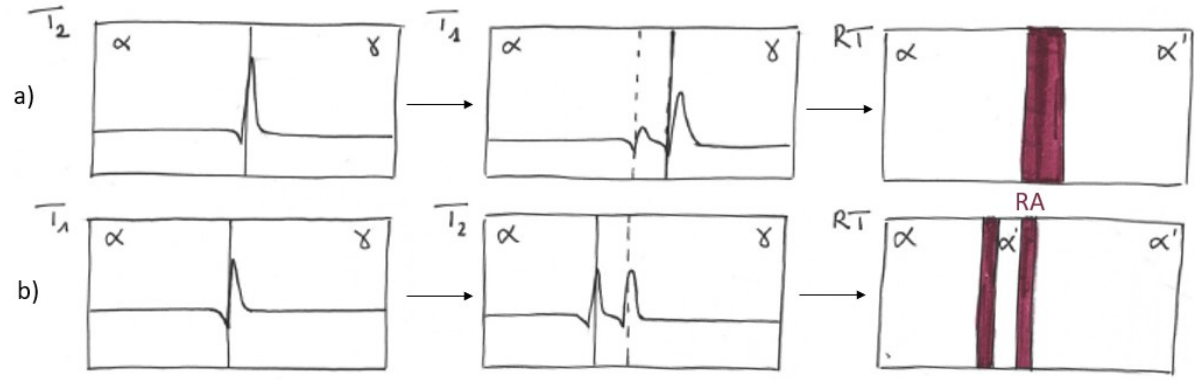

Figure 4.7: Schematics of the effects of the last cycle of CPPT on the final microstructure.

a similar amount of austenite as formed through the first cycle of route 2. Therefore the first cycle of route 1 is unnecessary. Moreover, the extra cycle in route 2 might help widen the Mn-enriched zone created at the austenite grains boundaries, hence in the following only CPPT heat treatments based on route 2 will be applied to samples with more than 4wt.%Mn.

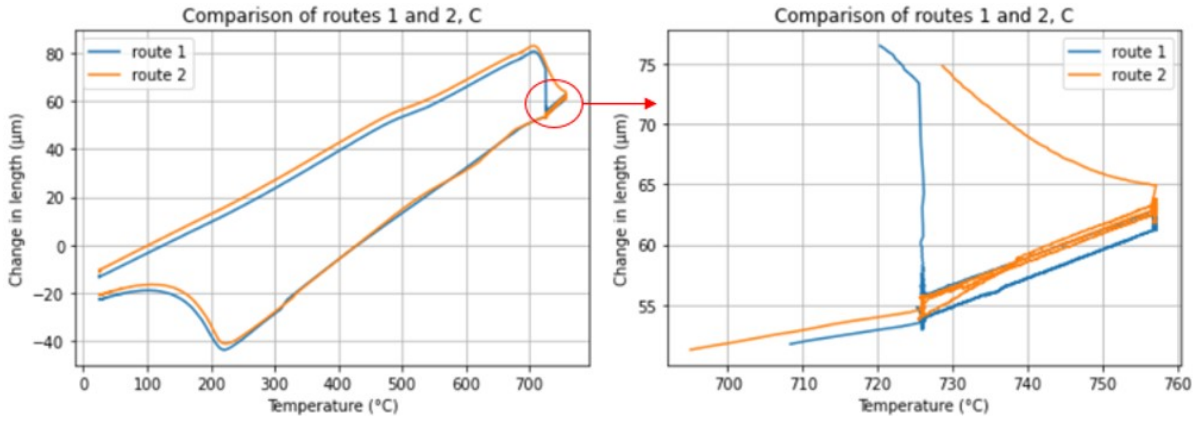

Figure 4.8: Comparison of the dilatometry curves of C from routes 1 and 2, with $T_1 = 726°C$ and $T_2 = 757°C$.

4.3. Selected heat treatments

For each type of sample, CPPT heat treatments with varying thermal parameters have been done. Isothermal intercritical annealings of 20 mins at T_1, starting from a fully martensitic microstruture, will serve as comparison for the CPPT heat treatments' results for the 6Mn and 6MnNi samples. All experiments discussed in the following sections are gathered in Table 4.4.

Name	Route	T_1	T_2	$T_{gap} = \|T_1 - T_2\|$	Cooling/heating rate
2Mn-50	3	690°C	740°C	50°C	10°C/s
2Mn-80	3	660°C	740°C	80°C	10°C/s
4Mn-r2-1	2	710°C	725°C	15°C	10°C/s
4Mn-r2-2	2	715°C	735°C	20°C	10°C/s
4Mn-r3	3	680°C	720°C	40°C	10°C/s
6Mn-10Cps	2	680°C	700°C	20°C	10°C/s
6Mn-5Cps	2	680°C	700°C	20°C	5°C/s
6Mn-an1	−−	680°C	−−	−−	10°C/s
6Mn-an2	−−	710°C	−−	−−	10°C/s
6Mn-an3	−−	680°C	700°C	−−	10°C/s
6MnNi-r2	2	680°C	700°C	20°C	10°C/s
6MnNi-an1	−−	670°C	−−	−−	10°C/s
6MnNi-an2	−−	680°C	700°C	−−	10°C/s

Table 4.4: Selected samples and heat treatments

5

Outcome of the selected heat treatments

In this section, the results obtained from the experiments recorded in Table 4.4 are developed. They are organized by chemical composition.

5.1. 2Mn

Both samples 2Mn-50 and 2Mn-80 have been submitted to a route 3 CPPT heat treatment. The only variation is the temperatures selected as T_1, to be able to observe the changes brought forth by a gap in temperature of 50°C and 80°C.

The dilatometry curves recorded during the heat treatments are shown in Figure 5.1. During the first and second cycles, 2Mn-80 has respectively more ferrite growth and more austenite growth than 2Mn-50. Thermodynamically, a higher volume fraction of ferrite will be formed at a lower intercritical temperature for a same chemical composition, and therefore more $\alpha \rightarrow \gamma$ transformation will happen when heating to an higher intercritical temperature. During the third cycle, as both samples have a similar volume fraction of austenite after annealing at T_2, they now show a similar ferrite growth. The recorded M_s temperature differs for the two samples, with $M_s = 300°C$ for 2Mn-50 and $M_s = 250°C$ for 2Mn-80. Therefore, an increase in the temperature gap between T_1 and T_2 might also increase the partitioning of Mn in γ, and might lead to a higher volume fraction of RA at room temperature.

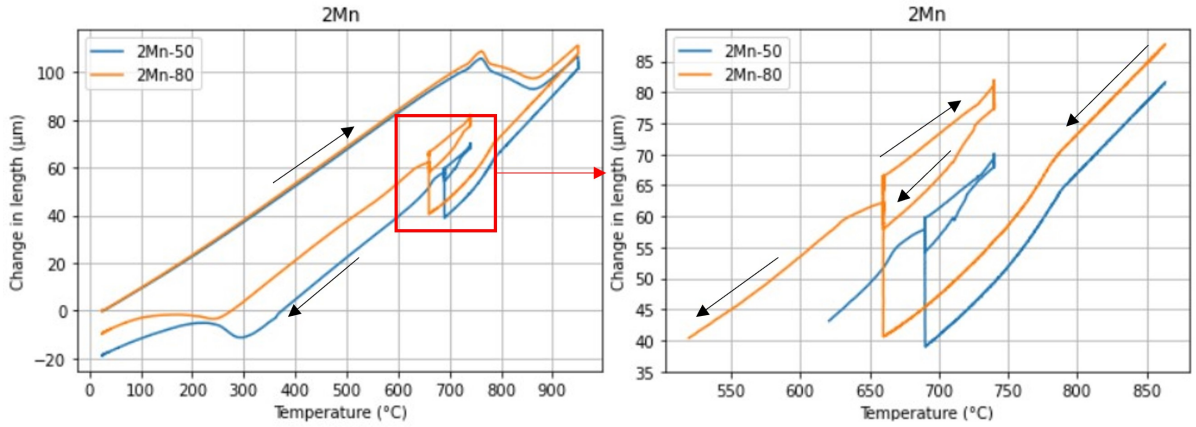

Figure 5.1: Dilatometry curves for 2Mn-50 and 2Mn-80.

The microstructures obtained at room temperature for 2Mn-50 and 2Mn-80 are presented in Figure 5.2. Both samples present coarse martensite islands, the majority of which have a diameter of 15μm. Ferrite

grains are equiaxed and on average smaller than the martensite grains, with diameters around 5μm. This morphology of martensite is expected from step quenched steels, which means steels that have first been fully austenitized, then subjected to an isothermal intercritical annealing, and finally quenched to room temperature [31]. The difference in diameters between ferrite and martensite grains can be explained by the prior fully austenitized state of the samples. This results in an important nucleation of ferrite grains when cooling to an intercritical temperature, but the annealing time is not sufficient for them to grow more. A 40-60% ratio between the volume fractions of ferrite and martensite can be observed on the SEM micrograph of 2Mn-50 (Figure 5.2a), with the ferrite grains being equiaxed and on average half the size of the martensite grains. 2Mn-50 presents a 35 to 75% ratio between the volume fractions of ferrite and martensite, and more small (2μm of diameter) and isolated martensite grains than for 2Mn-50.

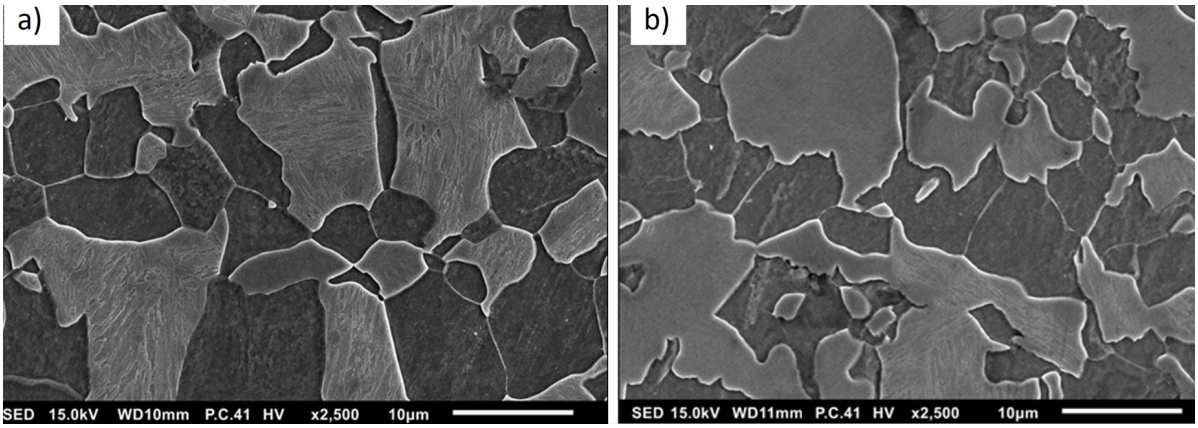

Figure 5.2: SEM micrographs of a) 2Mn-50 and b) 2Mn-80

SEM observations do not differentiate martensite and RA grains. Therefore, XRD analysis were made to determine the volume fraction of RA at room temperature in 2Mn-50 and 2-Mn80, the results of which are presented in Table 5.1. XRD analysis do not separate martensite grains from ferrite grains, and for both samples the combined volume fractions of ferrite and martensite is 99%. The remaining 1.5% and 1.6% respectively for 2Mn-50 and 2Mn-80 have been identified as RA. This very small volume fraction was expected due to the low Mn concentration of the samples, and it seems that a variation in the temperature gap between T_1 and T_2 for 2wt.% Mn samples do not impact the volume fraction of austenite stabilized at room temperature.

Sample	Ferrite/Martensite wt.%	Austenite wt.%
2Mn-50	0.99	0.015
2Mn-80	0.99	0.016

Table 5.1: Results of XRD analysis on 2Mn-50 and 2Mn-80

5.2. 4Mn

The intercritical range of temperatures for 4Mn could be determined during cooling and during heating. Therefore, both route 2 and route 3 might result in interfacial RA. Figure 5.3 shows the dilatometry curves obtained for 4Mn-r2-1, 4Mn-r2-2 and 4Mn-r3. The T_1 and T_2 temperatures used for 4Mn-r2-2 are higher than for 4Mn-r2-1, but both samples present similar changes in length during each annealing cycle. The dilatometry curve of 4Mn-r3 did not record any austenite growth happening at T_2, and only ferrite growth can be observed during the three cycles of route 3. This might be due to the low kinetics of ferrite growth when cooling to an intercritical temperature from a fully austenitized sample with high a Mn concentration. After the first annealing at T_1, the ferrite growth is not finished, and continues through the second cycle at T_2. The change of length of 4Mn-r3 observed at the third cycle (T_1) is

almost negligible, meaning that the sample has reached a state of equilibrium. This also means that the α/γ interface did not go back and forth in this experiment, hence there cannot be a stabilization of austenite at the interface due to Mn-enrichment.

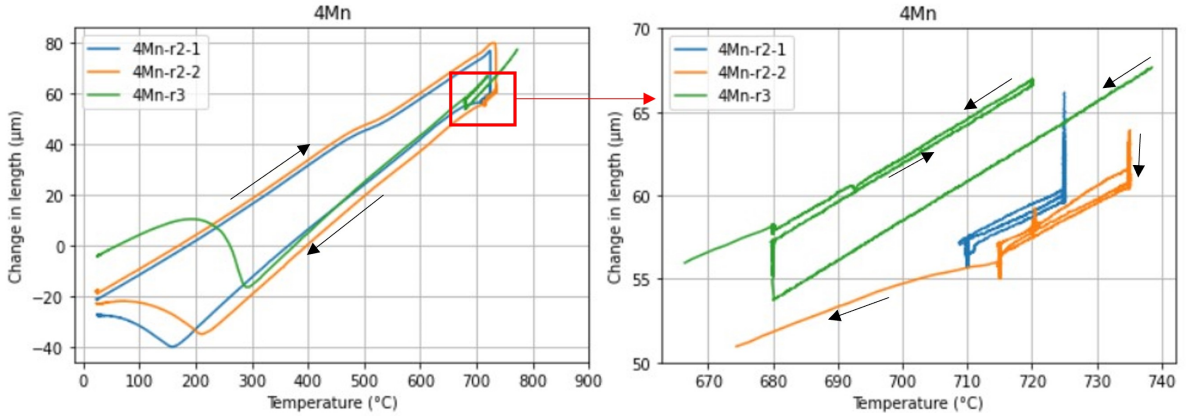

Figure 5.3: Dilatometry curves of 4Mn-r2-1, 4Mn-r2-2 and 4Mn-r3

Figures 5.4a and 5.4b are SEM micrographs of 4Mn-r2-1 and 4Mn-r2-2. Both are very similar, with needle-shaped ferrite grains surrounded by martensite. The slightly more important volume fraction of ferrite found in 4Mn-r2-1 can be attributed to the lower temperatures T_1 and T_2 used during its heat treatment. 4Mn-r3 however has a microstructure comprised of coarse martensite islands with a few small ferrite grains in betweem them as can be seen in Figure 5.4c. The small volume fraction of ferrite seems to contradict the observed ferrite growth in the dilatometry curve of 4Mn-r3 shown in Figure 5.3.

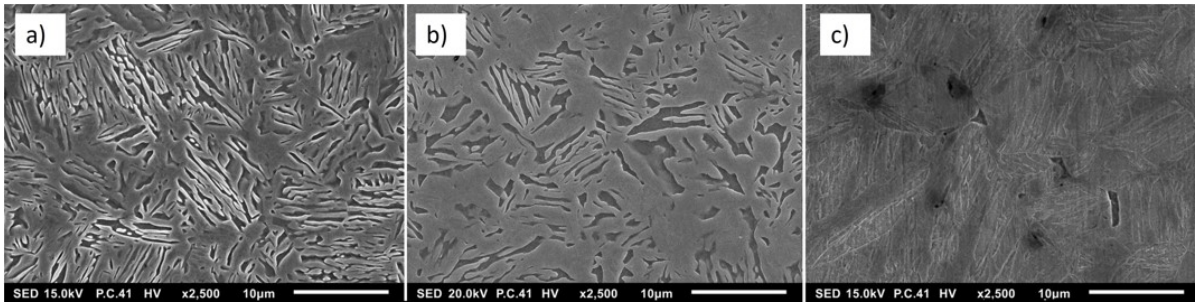

Figure 5.4: SEM micrograph of samples a) 4Mn-r2-1, b) 4Mn-r2-2 and c) 4Mn-r3

The strong similarities between Mn-r2-1 and Mn-r2-2 observed in the dilatometry curves (cf. Figure 5.3) as well as in the SEM micorgraphs (cf. Figure 5.4a and 5.4b) are also confirmed by XRD analysis. Both samples have a volume fraction of RA at room temperature of 4wt.%. No XRD analysis was performed on Mn-r3 as the probability of the stabilization of interfacial austenite due to the CPPT heat treatment is negligible, based on the dilatometry and microscopy results.

Sample	Ferrite/Martensite wt.%	Austenite wt.%
4Mn-r2-1	0.92	0.04
4Mn-r2-2	0.92	0.04

Table 5.2: Results of XRD analysis on 4Mn-an and 4Mn-r2-1

5.3. 6Mn

As previously mentioned in section 2.5.2, the manganese concentration in austenite must be at least 14.13wt.% to lower the M_s temperature to room temperature (25°C) or below based on Mahieu's equation (cf. equation 2.1 [21]), and thus stabilize austenite at room temperature. By modelling CPPT heat treatments in ThermoCalc with the Dictra functionality, it is possible to estimate the concentration profile of Mn at the α/γ interface. The highest Mn concentration at the interface obtained was 13wt.% Mn for a CPPT heat treatment following route 2 with $T_1 = 680°C$ and $T_2 = 700°C$ for 6Mn, as shown in Figure 5.5. It is still less than the wanted 14.13wt.%, but it can be expected that the highest amount of interfacial retained austenite will be obtained through CPPT heat treatments on 6Mn. A depletion of Mn preceded by an slightly enriched Mn-zone can also be seen around 9μm inside the ferrite phase, which must be the position of the α/γ interface during annealing at T_2.

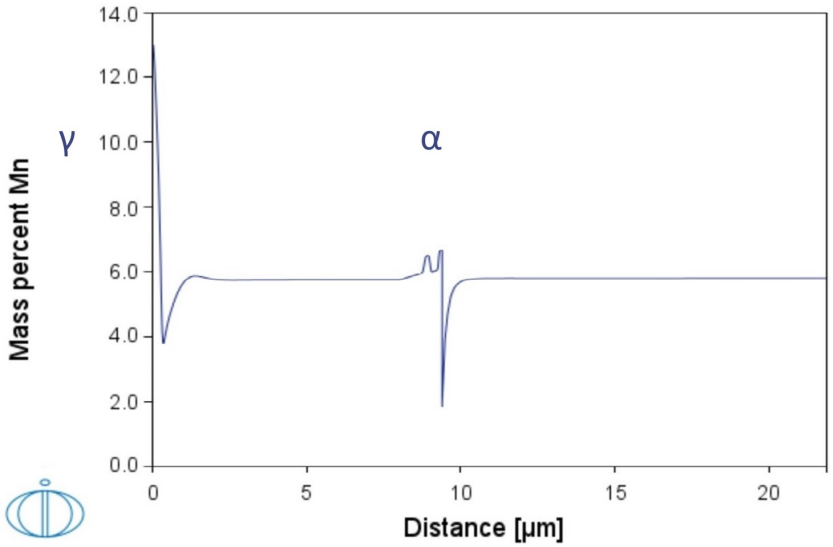

Figure 5.5: Modelling of the Mn concentration at the γ/α interface after a route 2 CPPT heat treatment with $T_1 = 680°C$ and $T_2 = 700°C$ on a 6Mn sample

In Figure 5.6 are the dilatometry curves of 6Mn-10Cps and 6Mn-5Cps. Both experiments were made following the same route and cycling between the same temperatures T_1 and T_2, but the cooling and heating rates between cycles change from 10°C/s for 6Mn-10Cps to 5°C/s for 6Mn-5Cps. Both curves show similar changes in length during the annealing cycles, recording a total change in length of around 2μm. It is doubtful whether the 10μm movement of the interface found through modelling in Figure 5.5 can be reproduced experimentally. The M_s temperature which can be extracted from the dilatometry curves slightly changes between 6Mn-10Cps and 6Mn-5Cps, with $M_s = 100°C$ and $M_s = 90°C$ respectively.

The resulting microstructures from the heat treatments recorded in Figure 5.6 are presented in Figure 5.7. Both samples have fine needle-shaped ferrite grains surrounded by martensite or RA. The ferrite grains of 6Mn-5Cps are on average wider than the ones in 6Mn-10Cps, but this difference might be due to local disparities in Mn concentrations due to Mn bandformations.

Isothermal intercritical annealing experiments were also performed at different holding temperatures to provide a comparison to samples treated by CPPT. All of the following samples have previously been fully austenitized for 5 mins at 950°C and then quenched to obtain a fully martensitic starting microstructure. 6Mn-an1 and 6Mn-an2 were isothermally intercritically annealed for 20 mins at 680°C and 710°C respectively. It is notable that a M_s temperature can't be determined from the dilatometry curve of 6Mn-an1, which seems to indicate that $M_s < 25°C$. Meanwhile, the curve of 6Mn-an2 very clearly shows that the $\gamma \rightarrow \alpha'$ transformation starts at $M_s = 150°C$ for this sample. 6Mn-an3 was intercritically annealed for a total time of 40 mins, first at 700°C and then at 680°C for 20 mins each. It can be seen

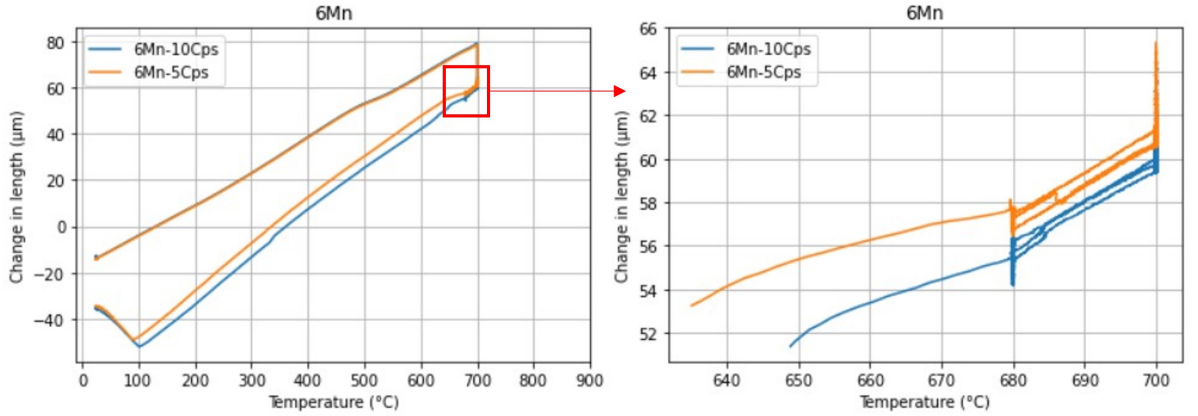

Figure 5.6: Dilatometry curves of 6Mn-10Cps and 6Mn-5Cps

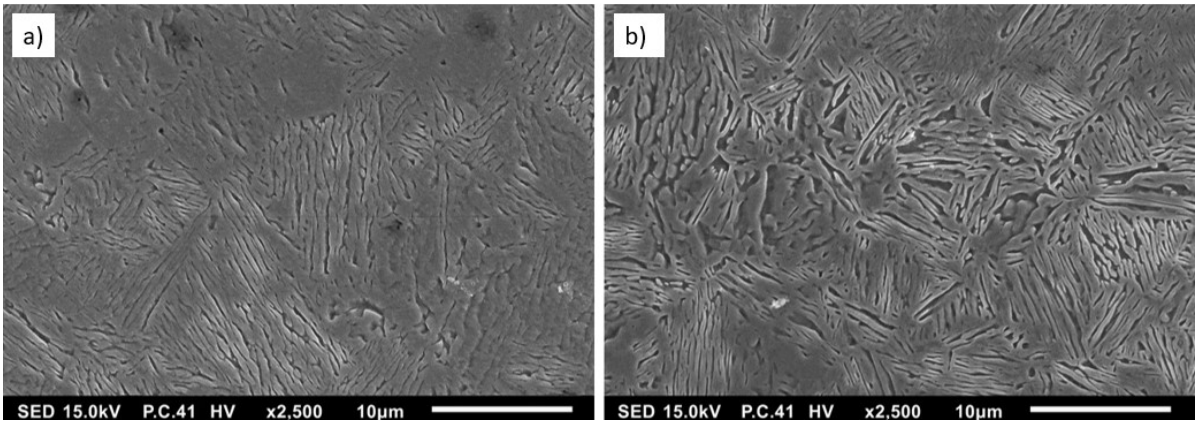

Figure 5.7: SEM micrographs of a) 6Mn-10Cps and b) 6Mn-5Cps

on Figure 5.6 that in this case the martensite transformation starts at $M_s = 100°C$.

The SEM micrographs of the annealed 6Mn samples can be observed on Figure 5.9. All the annealed samples have a microstructure comprised of narrow needle-shaped ferrite grains surrounded by martensite. 6Mn-an1 has a higher volume fraction of ferrite than 6Mn-an2 (cf. Figure 5.9a and 5.9b). This is due to 6Mn-an3 having a higher isothermal intercritical annealing temperature, favorizing the growth of austenite over ferrite. The micrograph of 6Mn-an3 presents longer ferrite grains than found for 6Mn-an1 and 6Mn-an2, as well as a more homogeneous repartition of the ferrite grains.

The volume fractions of RA for 6Mn-10Cps, 6Mn-5Cps, 6Mn-an1 and 6Mn-an3 were determined by XRD analysis and are gathered in Table 5.3. 6Mn-10Cps and 6Mn-5Cps have very similar volume fractions of RA, around 14 wt.%. After 40 mins of annealing between 700°C and 680°C, 6Mn-an3 also resulted in 14 wt.% of RA. However, it is most probable that the shape of the austenite grains stabilized at room temperature is different from the RA in 6Mn-10Cps and 6Mn-5Cps. An unexpected result of this analysis is the 43wt.% of RA obtained by annealing for 20 mins at 680°C (6Mn-an1). A new phase has been found through the XRD measurements but has yet to be identified with certainty. The closest match was a FeMn compound, which could hint towards a cementite phase.

EBSD analysis were performed on 6Mn-5Cps and 6Mn-an1 to locate and identify the shape of the RA grains. Figure 5.10a shows that RA grains (FCC) are very small (<1μm) and seem blocky or isolated. However, only 0.5wt.% of RA was identified in 6Mn-5Cps, which is very different from the results of the XRD analysis. The RA grains detected in 6Mn-an1 also have diameters smaller than 1μm, and a volume fraction of 3wt.%.

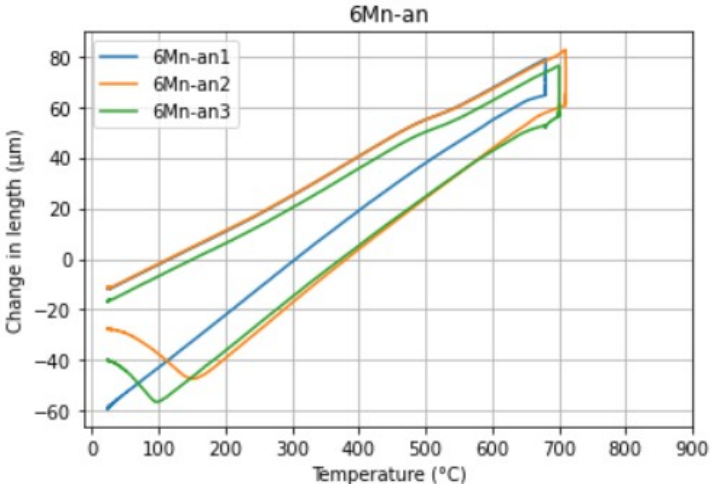

Figure 5.8: Dilatometry curves of 6Mn-an1, 6Mn-an2 and 6Mn-an3

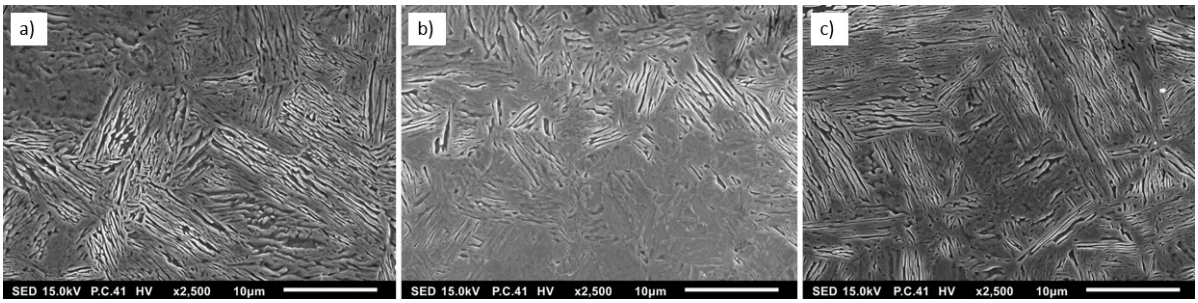

Figure 5.9: SEM micrographs of a) 6Mn-an1, b) 6Mn-an2 and c) 6Mn-an3.

The extent of the Mn-partitioning in γ can be computed based on the M_s value extracted from the dilatometry curves by using Mahieu's equation (cf. equation 2.1 [21]). However, the carbon atoms are also partitioning from α to γ at intercritical temperatures, which means that the concentration of C in γ before quenching is greater than the reported initial concentration of C. It is assumed that the concentration of C in α is null, and that all carbon atoms have partitioned to γ after a 1h20mins CPPT heat treatment in the intercritical range of temperatures. The volume fraction of α in 6Mn-5Cps has been estimated through the software ImageJ to 11.2wt.%. The initial concentration of carbon was 0.19wt.%. Therefore the concentration of carbon in γ before quenching is 0.19*100/88.8 = 0.21wt.% C. By applying Mahieu's equation to a M_s of 90°C for 6Mn-5Cps (cf. Figure 5.6), the average manganese concentration in γ before quenching is 11.5wt.%. Due to Mn-partitioning at the austenite side of the α/γ interface, the concentration in Mn at the borders of the austenite grains should be higher than in their centers.

EDS mapping was performed on 6Mn-5Cps to observe the variations in Mn concentration. As can be seen in Figure 5.11a, the Mn mapping shows a very homogeneous Mn concentration. However, longer individual spectra acquisitions (cf. Figure 5.11b) do find variations in the Mn concentrations. The point with the lowest Mn concentration is 002 with 2.93wt.%, at the border between a ferrite grain and a martensite/RA grain. The highest Mn concentration is achieved at 008 with 7.52wt.% and is also located at the interface between a ferrite grain and a martensite/RA grain. These measurements could relate respectively to the depletion and enriched zones forming at the α/γ interface due to Mn-partitioning. The average carbon concentration is 8.97wt.%, which is very different from the initial 0.19wt.% C. These high values might be due to the presence of cementite or from environmental factors.

Sample	Ferrite/Martensite wt.%	Austenite wt.%	FeMn wt.%
6Mn-10Cps	0.81	0.14	0.05
6Mn-5Cps	0.83	0.13	0.04
6Mn-an1	0.52	0.43	0.04
6Mn-an3	0.81	0.14	0.04

Table 5.3: Results of XRD analysis on 6Mn-10Cps, 6Mn-5Cps, 6Mn-an1 and 6Mn-an3

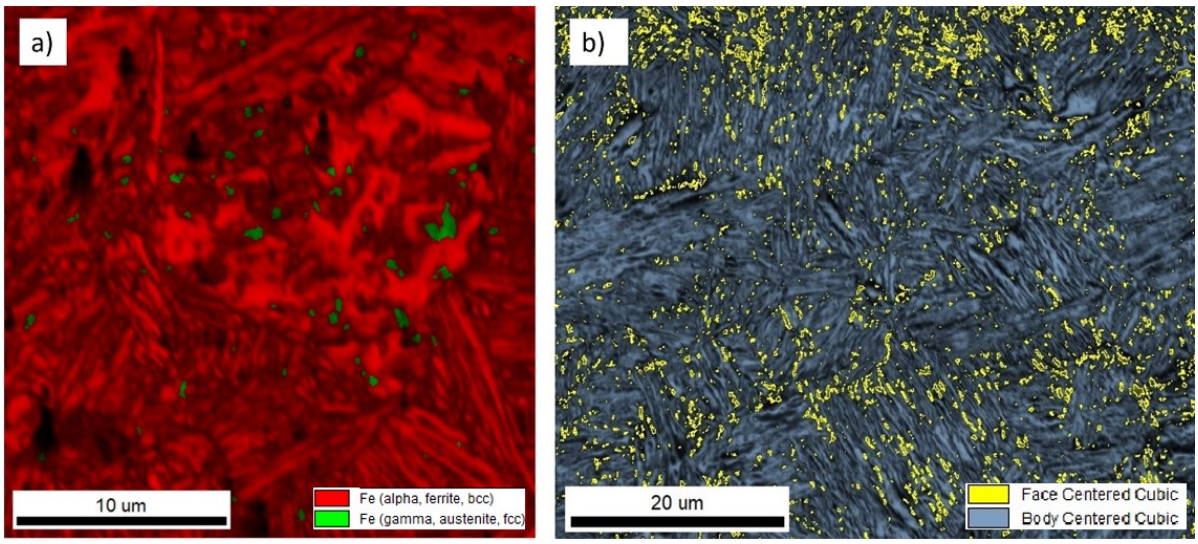

Figure 5.10: EBSD analysis on a) 6Mn-5Cps and b) 6Mn-an1

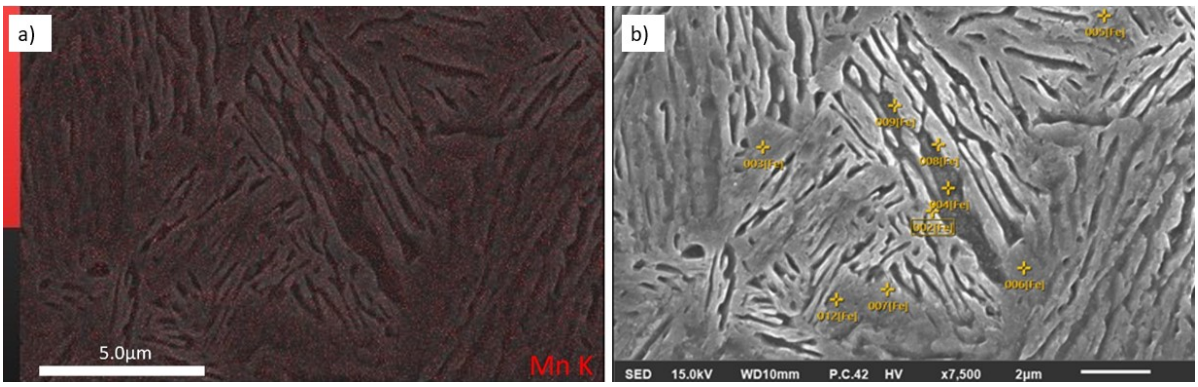

Figure 5.11: EDS mapping and spectra on 6Mn-5Cps at x7500 magnification

Numero	Fe wt.%	C wt.%	Mn wt.%	Si wt.%
002	88.67	7.71	2.93	0.70
003	85.71	8.70	4.31	1.29
004	85.68	9.00	4.40	0.92
005	83.41	9.57	6.19	0.83
006	84.60	8.73	5.38	1.28
007	81.78	9.93	6.78	1.51
008	82.42	9.39	7.52	0.67
009	85.43	9.30	4.35	0.92
012	77.10	15.78	6.22	0.89
Average	84.46	8.97	5.54	1.02
Deviation	3.51	3.06	1.39	0.26

Table 5.4: EDS quantitative analysis at different points of 6Mn-5Cps.

5.4. 6MnNi

The behaviour of 6MnNi is difficult to predict. As it has a high concentration in Mn, it should be able to form a relatively high volume fraction of RA, similarily to 6Mn samples. However, the presence of Ni complicates the determination of the Ac_1 and Ac_3 temperatures, as seen in section 4.1.2, and might also affect the stabilization of austenite at room temperature. Based on the Ac_1 and Ac_3 temperatures extracted from the slow cooling experiment, T_1 and T_2 have been respectively fixed at 680°C and 700°C for 6MnNi-r2. The resulting dilatometry curve is displayed in Figure 5.12, and reaches its M_s temperature at 170°C. The observed maximum change of length during a cycle is smaller than $1\mu m$, and there might not be sufficient movement of the interface to widen the Mn-ennriched region created by Mn-partitioning.

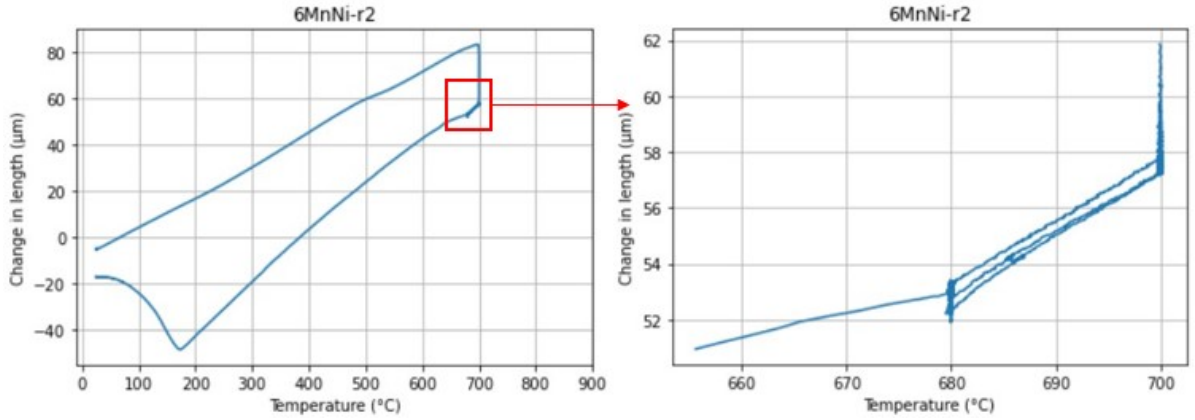

Figure 5.12: Dilatometry curve of 6MnNi-r2

6MnNi-an1 was isothermally annealed for 20 mins at 670°c and 6MnNi-an2 was annealed first at 700°C for 20 mins and then at 680°C for 20 mins. 6MnNi-an1 does not reach its M_s before room temperature, but 6MnNi-an2 starts the $\gamma \rightarrow \alpha'$ transformation at $M_s = 180°C$ (cf. Figure 5.13).

The resulting microstructures of 6MnNi-r2 and 6MnNi-an1 are displayed in Figure 5.14a and 5.14b respectively. Almost no ferrite growth can be observed for 6MnNi-r2, which hints to CPPT temperatures too high. 6MnNi-an1 however, shows fine elongated ferrite grains surrounded by martensite.

XRD analysis were performed on 6MnNi-r2 and 6MnNi-an1 to determine their volume fractions of RA at room temperature. It can be seen in Table 5.5 that only 4wt.% of austenite has stabilized at room temperature for 6MnNi-r2, while 47wt.% of RA has been found in 6MnNi-an1. Furthermore, the unidentified FeMn phase remains unaccounted for in 6MnNi-r2, but it is not the case for 6MnNi-an1 in which it has a volume fraction of 3wt.%. It can be expected that a higher volume fraction of RA could be

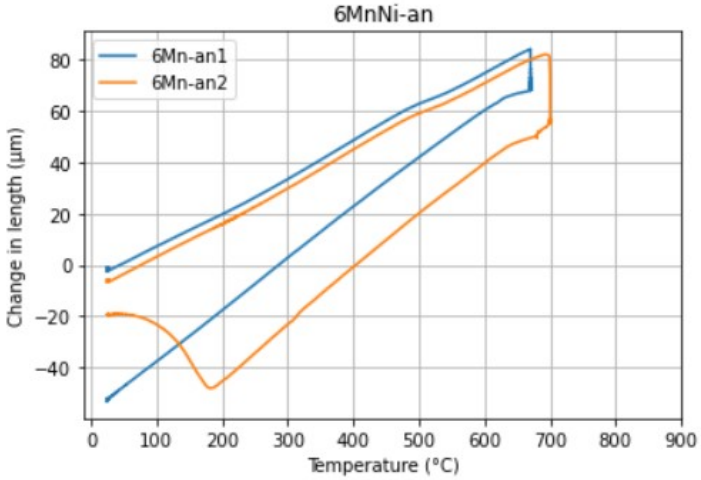

Figure 5.13: Dilatometry curves of 6MnNi-an1 and 6MnNi-an2.

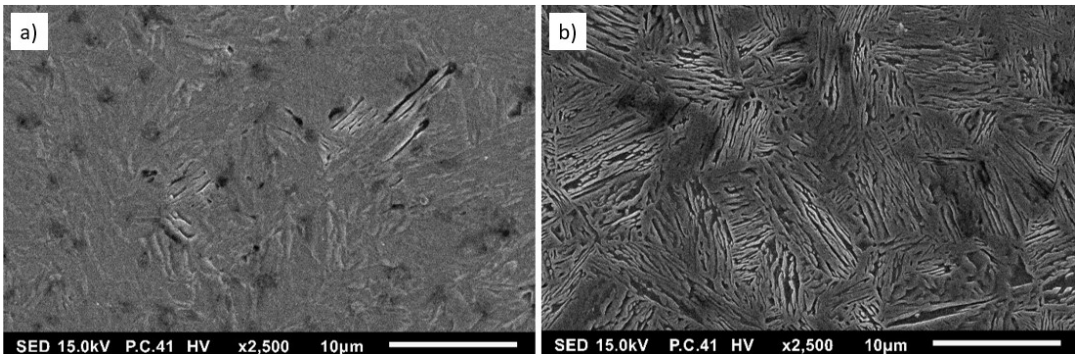

Figure 5.14: SEM micrographs of a) 6MnNi-r2 and b) 6MnNi-an1.

stabilized at room temperature through CPPT of 6MnNi by cycling in between lower temperatures than the ones selected form 6MnNi-r2.

Sample	Ferrite/Martensite wt.%	Austenite wt.%	FeMn wt.%
6MnNi-r2	0.96	0.04	– –
6MnNi-an1	0.50	0.47	0.03

Table 5.5: Results of XRD analysis on 6MnNi-r2 and 6MnNi-an1

6 Discussion

Based on the outcomes of the CPPT experiments realized during this thesis, the influence of the samples' chemical compositions and of the heat treatments' thermal parameters on the resulting microstructures are explored in this section. The stabilization of interfacial retained austenite at room temperature due to CPPT is evaluated, and the results from the isothermal intercritical annealing experiments are investigated.

6.1. Influence of the chemical composition

The chemical composition of the samples determined their CPPT routes based on the kinetics of austenite and ferrite growth. It also impacted the Mn concentrations attainable through Mn-partitioning, and therefore the volume fraction of RA at room temperature.

6.1.1. Ferrite and martensite morphologies

Both 2Mn and 4Mn samples were treated based on route 3. 2Mn-50, 2Mn-80 and 4Mn-r3 all present a similar microstructure comprised of coarse martensite islands formed in large prior austenite grains and of small equiaxed ferrite grains which nucleated at γ/γ interfaces. The prior austenite grains are bigger than the ferrite grains as the samples cooled to intercritical temperatures from full austenitization, allowing more growth of the austenite grains (cf. Figure 5.2a and 5.2b). However, 4Mn-r3 has very few small ferrite grains (cf. Figure 5.4c). This shows that the kinetics of ferrite growth with 4wt.%Mn are highly slowed down compared to 2wt.%Mn. As the volume fraction of ferrite obtained in 4Mn-r3 is almost negligible, route 3 was not used on samples with higher Mn concentrations.

4Mn, 6Mn and 6MnNi were submitted to CPPT heat treatments following route 2. In this case, the samples were heated up to intercritical temperatures from a fully martensitic microstructure. The resulting microstructure is very different from the one obtained with route 3. Martensite grains are not coarse and encased into prior austenite grains anymore, they form a sort of matrix around the ferrite grains. The ferrite grains are very narrow and elongated, in a needle-like shape reminiscent of martensite grains. During these heat treatments both ferrite and austenite grains nucleate from α'/α' interfaces and grow following the shape of already present martensite grains. The samples are not held at intercritical temperatures for a long enough time to allow the ferrite and austenite grains to widen.

The presence of an unknown phase identified as a FeMn compound was detected through XRD analysis for all 6Mn samples with a volume fraction of 4 or 5wt.%, and for 6MnNi-an1 with a volume fraction of 3wt.% (cf. Tables 5.3 and 5.5). This compound could be a cementite-ferrite aggregate, which would hint towards the use of T_1 temperatures below Ac_1. The absence of this phase in the results of the XRD analysis on 6MnNi-r2 is also of interest. As 6MnNi-r2 was subjected to higher temperatures than 6MnNi-an1, the formation of cementite-ferrite aggregates would have been inhibited. The results of the EDS spectra analysis on 6Mn-5Cps reported in Figure 5.11 and in Table 5.4 also seem to support

this theory as high concentration of carbon were detected, with an average of 8.97wt.%. These high concentrations could be due to the C-partitioning in cementite, but they also might have been impacted by environmental factors such as the carbon tape used to hold the samples during the EDS analysis.

The fact that 6MnNi contains nickel also complicates the issue. The T_1 and T_2 temperatures selected from the slow cooling experiment were most likely not adapted to obtain a DP steel after quenching as the resulting microstructure was mostly martensitic. It is probable that the addition of nickel complicates the extraction of the Ac_1 and Ac_3 temperatures from dilatometry curves, and thus that they need to be selected with extra precautions.

6.1.2. Stabilization of austenite at room temperature

As expected from the Mn profiles modelled through ThermoCalc, the highest volume fractions of RA obtained through CPPT were detected in 6Mn samples. XRD analysis detected a maximum of 1.6wt.%, 4wt.% and 14wt.% for 2Mn, 4Mn and 6Mn respectively (cf. Tables 5.1, 5.2 and 5.3). These variations should stem from the differences in the initial Mn concentration in these samples. As calculated through Mahieu's equation, a Mn concentration of approximately 14wt.% is necessary for the M_s temperature to be 25°C. Reaching this concentration at the α/γ interface through Mn-partitioning in 2Mn and 4Mn asks for a total partitioning of Mn from α to γ, which is especially unrealistic in the time frame of these heat treatments.

6MnNi-r2 only stabilized 4wt.% of austenite at room temperature despite its high Mn concentration (cf. Table 5.5). As previously mentioned, the resulting microstructure of 6MnNi-r2 contains very few ferrite grains, which hints to a mistake in the selection of T_1 and/or T_2. It can be expected that a CPPT heat treatment with more adapted temperatures will result in a higher volume fraction of ferrite. More Mn atoms would then be available to partition into austenite, which should increase the volume farction of RA detected at room temperature.

6.2. Influence of thermal parameters

Throughout this thesis, variations in the thermal parameters of the CPPT heat treatments were implemented to observe their impact on the volume fraction of RA present at room temperature.

2Mn-50 and 2Mn-80 have a 30°C difference in their temperature gaps ($|T_1 - T_2|$), and a variation of 0.1wt.% of RA was found between them at room temperature. An increased temperature gap should lead to bigger changes in the size of the austenite and ferrite grains. This means that the α/γ interface will travel a wider distance. To allow for the manganese spikes formed at the α/γ interface during each annealing cycle to merge and widen, this distance should not be too big as the Mn atoms from the previous spike would not be attracted towards the grain boundary. However, if the distance is too small, then the Mn spike can not widen enough to create a localized Mn-enriched zone at the border of the austenite grains which would stabilize into interfacial RA at room temperature. As 2Mn samples did not give the best results in terms of volume fraction of austenite stabilization at room temperature, it would be interesting to try a similar experiment on 6Mn samples. However, an increase in Mn concentration leads to a smaller temperature difference between Ac_1 and Ac_3. Therefore, selecting two sets of T_1 and T_2 temperatures for 6Mn such that their temperature gaps are sufficiently different, and while remaining between Ac_1 and Ac_3 becomes an arduous task.

The influence of higher or lower T_1 and T_2 temperatures with similar temperature gaps was studied through samples 4Mn-r2-1 and 4Mn-r2-2. The T_1 and T_2 temperatures of 4Mn-r2-1 are respectively 5°C and 10°C lower than for 4Mn-r2-2. This variation lead to a change in M_s from 160°C for 4Mn-r2-1 to 210°C for 4Mn-r2-2 due to the higher volume fraction of austenite in 4Mn-r2-2 before quenching. This is confirmed by the SEM micrographs of both samples in which a higher volume fraction of ferrite is present for 4Mn-r2-1 than for 4Mn-r2-2. Despite that, XRD analysis detected identical volume fractions of RA at room temperature for both samples. It can be assumed that an average Mn concentration of 4wt.% is not sufficient to stabilize interfacial austenite at room temperature through Mn-partitioning. It

would be of interest to realize a similar experiment on a sample with a higher Mn concentration such as 6Mn, but the narrowing of the intercritical range of temperatures complicates the selection of adequate T_1 and T_2.

Finally, the impact of the heating and cooling rates in-between cycles was studied through 6Mn-5Cps and 6Mn-10Cps, with respective rates of 5°C/s and 10°C/s. As the temperature gap between T_1 and T_2 in these experiments is only of 20°C, this corresponds to a 6 seconds elongation of the heat treatment applied to 6Mn-5Cps compared to 6Mn-10Cps. Due to this very minor change, no differences were expected between the microstructures of both samples. However, it can be seen in the SEM micrographs that the ferrite grains of 6Mn-10Cps are narrower and longer than those of 6Mn-5Cps. It is very probable that this change is due to Mn bandformations present in the initial material rather than from a variation in cooling/heating rates. However, a similar experiment with lower cooling/heating rates such as 0.1°C/s could have a strong influence of the resulting microstructure. If the rate is too low, it is also possible that the the α/γ interface mobility becomes too slow to leave a sufficient Mn concentration spike at its previous position.

The focus of this thesis is on the thermal stabilization of austenite at room temperature in medium Mn DP steels through CPPT treatments. However, mechanical and magnetic stabilization methods have also been established successfully [32][33][34][35]. Similar processes could be implemented in association with thermal stabilization methods to obtain an optima RA volume fraction at room temperature in medium Mn DP steels.

6.3. Stabilization of interfacial retained austenite

The volume fractions of RA at room temperature detected between the XRD analysis and the EBSD analysis for 6Mn-5Cps and 6Mn-an1 are highly different. For 6Mn-5Cps, XRD found 13wt.% against 0.5wt.% for EBSD. In the case of 6Mn-an1, 43wt.% of RA determined through XRD became 3wt.% through EBSD. This difference in results can be explained by the very fine microstructure of both samples. The SEM micrographs of both samples reveal very narrow and elongated ferrite grains surrounded by martensite/RA. The background of the EBSD acquisitions also show very chaotic and needle-shaped grains without distinguishing ferrite and martensite. During an EBSD acquisition, each grain boundary is surrounded by an area of uncertain identification due to the joining of two grains of dissimilar crystallographic orientations and phases. As the micorstructure of our samples is very fine, there is also a high amount of grain boundaries. This means that an important area might be wrongly identified. In the case of 6Mn-5Cps and 6Mn-an1, only the biggest grains of RA were detected, and their diameters are already smaller than 1μm. If interfacial RA is present in 6Mn-5Cps, its shape is most likely very narrow and elongated, rendering it almost impossible to detect through EBSD analysis. Therefore, while an important volume fraction of retained austenite could be obtained at room temperature through CPPT (13wt.% for 6Mn-5Cps based on the XRD analysis), it is at this time impossible to conclude on its interfacial character. Further characterization through Transmission Electron Micorscopy or Auger Electron Spectroscopy could help confirm the RA morphology.

6.4. RA obtained through annealing

6Mn-an1 and 6MnNi-an1 had volume fractions of retained austenite at room temperature exceding 40wt.%. Both samples were annealed for 20 mins at a low intercritical temperature (680°C for 6Mn-an1 and 670°C for 6MnNi-an1). This means that at these temperatures, there was more than 40wt.% of austenite. When quenching, no M_s temperatures were recorded in both dilatometry curves. Therefore, it can be assumed that the entirety of the austenite formed before quenching stabilized at room temperature, and that almost no martensite was formed upon quenching. The SEM micrographs of both samples show a high volume fraction of needle-shaped ferrite grains. As the starting microstructure of 6Mn-an1 and 6MnNi-an1 is fully martensitic, ferrite grains nucleated at α'/α' interfaces and grew alongside the martensite grains in narrow and elongated shapes. This provided a large quantity of nucleation sites for austenite grains at α/α and α/α' interfaces. Therefore, it is very likely that a high amount of austenite grains was formed. With a low intercritical annealing temperature, the austenite grains will

have remained relatively small and in between ferrite grains. This would lead to a high quantity of α/γ interfaces, at which Mn-partitioning would occur. If the austenite grains also remain narrow, then the Mn-enrichment of γ through partitioning and diffusion of Mn from α to γ will be enhanced. Hence, an important volume fraction of austenite would be stabilized after quenching at room temperature.

7

Conclusion

In this thesis, the possibility of interfacial austenite stabilization at room temperature in a medium Mn DP steel through a CPPT approach is explored. XRD analysis shows that 14wt.% of RA has been successfully obtained at room temperature in a Fe-5.8Mn-0.19C-1.4Si (wt.%) DP steel after four isothermal intercritical annealing cycles alternating between 700°C and 680°C. The mechanisms of Mn-partitioning characterizing the NPLE growth of austenite and the back and forth movements of the interface due to CPPT should have allowed the stabilization of interfacial austenite. However, the very fine resulting microstructure and the resolution limits of the EBSD analysis do not allow to conclude on the morphology of this RA.

High volume fractions (>40wt.%) of RA at room temperature were obtained after isothermal annealing experiments at fixed low intercritical temperatures. This can be attributed to the important amount of austenite nucleation sites generated by a fully martensitic starting microstructure.

During this study, it has been determined that the chemical composition and the initial microstructure of the sample have an important influence on the volume fraction of austenite stabilized at room temperature after CPPT heat treatments. Variations in thermal parameters of the CPPT heat treatment, such as the temperature gap between T_1 and T_2 or the cooling and heating rates in-between cycles, did not influence the volume fraction of RA obtained at room temperature. Further research is required to fully understand the mechanisms of austenite stabilization at room temperature through a CPPT approach.

References

[1] F. Badkoobeh, H. Mostaan, M. Rafiei, H. Bakhsheshi-Rad and F. Berto., 'Microstructural characteristics and strengthening mechanisms of ferritic-martensitic dual-phase steels: A review', *Metals*, vol. 12, no. 101, 2022.

[2] M. Soleimani, A. Kalhor and H. Mirzadeh., 'Transformation-induced plasticity (trip) in advanced steels: A review', *Materials Sience & Engineering A*, vol. 795, no. 140023, 2020.

[3] P. Prislupcak, T. Kvackaj, J. Bidulska *et al.*, 'Effect of retained austenite on plastic characteristics of dual phase steels', *Acta Metallurgica Slovaca*, vol. 28, no. 4, pp. 212–218, 2022.

[4] D. Saha, E. Biro, A. Gerlich and Y. Zhou., 'Influences of blocky retained austenite on the heat-affected zone softening of dual-phase steels', *Materials Letters*, vol. 264, no. 127368, 2020.

[5] J. Yi, K. Yu, I. Kim and S. Kim., 'Role of retained austenite on the deformation of an fe-0.07c-1.8mn-1.4si dual-phase steel', *Metallurgical Transactions A*, vol. 14, pp. 1497–1504, 1983.

[6] L. Giordano, P. Matteazzi, A. Tiziani and A. Zambon., 'Retained austenite variations in dual-phase steel after mechanical stressing and heat treatment', *Materials Science and Engineering A*, vol. 131, pp. 215–219, 1990.

[7] B. Hu, Q. Zheng, Y. Lu *et al.*, 'Stabilizing austenite via intercritical mn partitioning in a medium mn steel', *Scripta Materialia*, vol. 225, pp. 1–6, 2023.

[8] R. Varanasi, M. Lipinska-Chwalek, J. Mayer, B. Gault and D. Ponge., 'Mechanisms of austenite growth during intercritical annealing in medium manganese steels', *Scripta Materialia*, vol. 206, pp. 1–7, 2022.

[9] D. Edmonds, K. He, F. Rizzo, B. D. Cooman, D. Matlock and J. Speer, 'Quenching and partitioning martensite – a novel steel heat treatment', *Materials Science and Engineering A*, vol. 438-440, pp. 25–34, 2006.

[10] A. Clarke, J. Speer, M. Miller *et al.*, 'Carbon partitioning to austenite from martensite or bainite during the quench and partition (q&p) process: A critical assessment', *Acta Materialia*, vol. 56, pp. 16–22, 2008.

[11] H. Farahani, W. Xu and S. van der Zwaag., 'A novel approach for controlling the band formation in medium mn steels', *Metallurgical and Materials Transactions A*, vol. 49, pp. 1998–2010, 2018.

[12] Z. Nasiri, S. Ghaemifar, M. Naghizadeh and H. Mirzadeh., 'Thermal mechanisms of grain refinement is steels: A review', *Metals and Materials International*, vol. 27, pp. 2078–2094, 2021.

[13] H. Niakan and A. Najafizadeh., 'Effect of niobium an drolling parameters on the mechanical properties of microstructure of dual phase steels', *Materials SCience and Engineering A*, vol. 527, pp. 5410–5414, 2010.

[14] C. Guo, L. Hao, S. Li, Y. Kang and Y. An., 'Effect of microstructure quenched around A_{c3} on the damage behavioor in 0.087c-1.35mn steel', *Journal of Materials Research and Technology*, vol. 8, no. 6, pp. 5103–5113, 2019.

[15] W. Jeong and C. Kim., 'Communications on the isolated retained austenite in a dual-phase steel', *Metallurgical Transactions A*, vol. 18, pp. 933–934, 1987.

[16] H. DeVoe, *Thermodynamics and Chemistry - Second Edition*. Pearson Education, Inc., 2019, pp. 425–433.

[17] F. Maresca, V. Kouznetsova and M. Geers, 'On the role of interlath retained austenite in the deformation of lath martensite', *Modelling and Simulation in Materials SCience and Engineering*, vol. 22, pp. 1–21, 2014.

[18] H. Li, L. Duan, Z. Mi, Z. Zhao and D. Tang., 'Distribution and evolution of retained austenite in dual-phase steel', *Journal of South China University of Technology (Natural Sience)*, vol. 41, no. 10, pp. 92–96, 2013.

[19] J. Benzing, A. K. da Silva, L. Morsdorf *et al.*, 'Multi-scale characterization of austenite reversion and martensite recovery in a cold-rolled medium-mn steel', *Acta Materialia*, vol. 166, pp. 512–530, 2019.

[20] J. Mahieu, J. Maki, B. D. Cooman and S. Claessens., 'Phase transformation and mechanical properties of si-free cmnal transformation-induced plasticity-aided steel', *Metallurgical and Materials Transactions A*, vol. 33, pp. 2573–2580, 2002.

[21] E. D. Moor, D. Matlock, J. Speer and M. Merwin., 'Austenite stabilization through manganese enrichment', *Scripta Materialia*, vol. 64, pp. 185–188, 2011.

[22] H. Bhadeshia and R. Honeycombe., *Steels: Structure and Properties*. Elsevier, 2017, pp. 68–73, 112–115.

[23] H. Chen, B. Appolaire and S. van der Zwaag., 'Application of cyclic partial phase transformations for identifying kinetic transitions during solid-state phase transformations: Experiments and modeling', *Acta Materialia*, vol. 59, pp. 6751–6760, 2011.

[24] H. Chen, R. Kuziak and S. van der Zwaag., 'Experimental evidence of the effect of alloying additions on the stagnant stage length during cyclic partial phase transformations', *Metallurgical and Materials Transactions A*, vol. 44, pp. 5617–5621, 2013.

[25] Y. Liu, P. China, F. Sommer and E. Mittemeijer., *Phase Transformations in Steels*. Woodhead Publishing, 2012, vol. 1, ch. 9 - Nature and kinetics of the massive austenite-ferrite phase transformations in steels, p. 315.

[26] E. Gamsjäger, H. Chen and S. van der Zwaag., 'Application of the cyclic phase transformation concept for determining the effective austenite/ferrite interface mobility', *Computational Materials Science*, vol. 83, pp. 92–100, 2014.

[27] H. Chen, E. Gamsjäger, S. Schider, H. Khanbareh and S. van der Zwaag., 'In situ observation of austenite-ferrite interface migration in a lean mn steel during cyclic partial phase transformations', *Acta Materialia*, vol. 61, no. 7, pp. 2414–2424, 2013.

[28] H. Chen and S. van der Zwaag., 'Application of the cyclic phase transformation concept for investigating growth kinetics of solid-state partitioning phase transformations', *Computational Materials Science*, vol. 49, pp. 801–813, 2010.

[29] H. Chen and S. van der Zwaag., 'An overview of the cyclic partial austenite-ferrite transformation concept and its potential', *Metallurgical and Materials Transactions A*, vol. 48, pp. 2720–2729, 2016.

[30] H. Faharani, W. Xu and S. van der Zwaag., 'Prediction and validationof the austenite phase fraction upon intercritical annealing of medium mn steels', *Metallurgical and Materials Transactions A*, vol. 46, pp. 4978–4985, 2015.

[31] B. R. Kumar, N. Patel, K. Mukherjee, M. Walunj, G. Mandal and T. Venugopalan., 'Ferrite channel effect on ductility and strain hardenability of ultra high strength dual phase steel', *Materials Science & Engineering A*, vol. 685, pp. 187–193, 2017.

[32] B. He, M. Wang and M. Huang, 'Resetting the austenite stability in a medium mn steel via dislocation engineering', *Metallurgical and Materials Transactions A*, vol. 50, pp. 2971–2977, 2019.

[33] T. Miura, R. Ueji and H. Fujii, 'Stabilization of retained austenite in cr-mo steel by microalloying and friction stir welding', *Proceedings of the 1st International Joint Symposium on Joining and Welding*, pp. 107–110, 2013.

[34] Z. Li, K. Li, C. Qian *et al.*, 'Effect of pulsed magnetic field on retained austenite of quenched 8cr4mo4v steel under cryogenic condition', *Journal of Materials Research ad Technology*, vol. 23, pp. 5004–5015, 2023.

[35] Y. Dolgachev, V. Pustovoit, M. Egorov and V. Lebedenko, 'Effect of magnetic state of austenite on thermodynamics and kinetics of martensite transformation in steels', *Metallurgist*, vol. 66, no. 10, pp. 63–69, 2023.